

*Mechanics of Subglacial Hydrology
under Supraglacial Lakes and Ice
Stream Shear Margins*

A THESIS PRESENTED
BY
MATHEUS C. FERNANDES
TO
THE SCHOOL OF ENGINEERING AND APPLIED SCIENCES

IN PARTIAL FULFILLMENT OF THE REQUIREMENTS
FOR THE DEGREE OF
MASTERS OF ENGINEERING
IN THE SUBJECT OF
ENGINEERING SCIENCES - MATERIAL SCIENCE AND
MECHANICAL ENGINEERING

HARVARD UNIVERSITY
CAMBRIDGE, MASSACHUSETTS
MAY 2015



© 2015 - *MATHEUS C. FERNANDES*
ALL RIGHTS RESERVED.

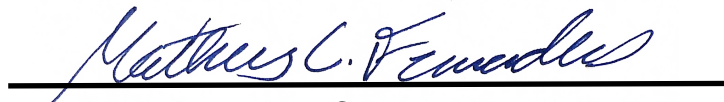
Thesis advisors:
Professor James R. Rice (Primary)
Professor Katia Bertoldi (Reader)

Author:
Matheus C. Fernandes

Mechanics of Subglacial Hydrology under Supraglacial Lakes and Ice Stream Shear Margins

ABSTRACT

This thesis is broken down into two parts, both of which are focused on the mechanics of subglacial hydrology. The first part describes the opening behavior of a crack under a supraglacial lake, where a Finite Element Method model is presented to obtain the opening profile of a crack undergoing hydrostatic tension in an infinite power law creep material. The second part focuses on creating a numerical model for the opening diameter of Röthlisberger channels in ice stream shear margins, where antiplane strain rates are superimposed on in-plane stresses.



Matheus C. Fernandes

Cambridge, MA 02138
05/01/2015

Contents

1	INTRODUCTION	1
1.1	Structure of Thesis	1
1.2	Supraglacial Crack-Crevasse	2
1.3	Röthlisberger Channel with Anti-plane Shear	3
2	SOLUTION FOR THE AVERAGE OPENING OF A CRACK IN A POWER-LAW CREEPING SOLID	4
2.1	Abstract	5
2.2	Introduction	6
2.3	Numerical Model Description	11
2.4	Numerical Validation	13
2.5	Exploring the Double HRR Opening Solution	20
2.6	Results	21
2.7	Discussion	24
2.8	Conclusion	26
3	TIME SCALE FOR RAPID DRAINING OF A SURFICIAL LAKE INTO THE GREENLAND ICE SHEET	28
3.1	Abstract	29
3.2	Introduction	30
3.3	Analysis	33
3.4	Application to basal fracture propagation	38

3.5	Coupling to lake water supply to the bed by a vertical crack-crevasses system	41
3.6	Estimating the time scale for lake drainage	48
3.7	Conclusions	53
4	RÖTHLISBERGER CHANNELS UNDER ANTIPLANE SHEAR	58
4.1	Abstract	58
4.2	Introduction	60
4.3	Analysis	64
4.4	Results	72
4.5	Implications for Röthlisberger analysis	90
4.6	Conclusion	96
5	CONCLUSION	98
A	ADDITIONAL MATERIAL FOR CHAPTER 2	101
A.1	Nye Solution for a Finite Body	101
A.2	Alternate Derivation of Opening Rate Approximation . . .	107
B	ADDITIONAL MATERIAL FOR CHAPTER 4	111
B.1	Method for Solving Anti-plane Solution	111
B.2	Scaling Relationship for Radial Average Velocity	114
	REFERENCES	122

Listing of figures

2.1	Figure illustrates the non-dimensional y-opening rate of a circular shape cavity and of a crack shaped cavity within an infinite power law creep medium. The cavity, in the infinite medium undergoes a net hydrostatic tension applied as a far-field boundary condition. The y-opening rate of both, a circular cavity and a crack, are dependent on the x position from the center of the cavity.	9
2.2	Zoomed in figure of FEM discretization near the crack tip, where the crack face is highlighted as the horizontal gray line. A quarter point method is used for the node placement near the crack tip to capture the square root singularity, and the crack tip is modeled as a collapse ring of quadrilateral elements to capture the $1/r$ singularity. . .	14
2.3	This plot validates the steady state fully plastic creep regime of the model. The simulation time is nondimensionalized using the timescale described in eq. (2.8). The velocity is nondimensionalized using the known Nye solution for the circular channel. In this semi-log plot, it is apparent that the time required for the elastic relaxation to have negligible impact on the steady state solution is around $10^3 * t_R$	15

2.4	Benchmark of numerical model to analytic solution. This figure shows the numerical results overlaid on the Nye analytic solution for a crack under linear creep material model. The numerical results closely contour the analytic solution conveying little to no error.	16
2.5	Error analysis comparing numerical simulation to known analytic solution. This figure shows the percent error calculated as $\%Error = \frac{\dot{u}^{Nye} - \dot{u}^{comp}}{\dot{u}^{Nye}} * 100\%$, where \dot{u}^{Nye} is the analytical Nye solution eq. (2.2) and \dot{u}^{comp} are the numerical results for each node seen in fig. 2.4.	17
2.6	This is a benchmark for the numerical results assuming a nonlinear power law rheology. The near crack tip region closely contours the numerical results attained from the simulation. This proves that the mesh in the crack tip region is adequately constructed. In the region away from the crack tip singularity (more than $\sim 20\%$ of crack length away from the tip), the HRR solution does not accurately describe the stress and strain fields, thus it cannot serve as a benchmark for the model in that region. . .	19
2.7	Plotted is the nondimensional double HRR solution for the opening of a crack in a power law creep material with $n = 3$ (eq. (2.17)) as compared to the nondimensional numerical simulation for $n = 3$	21

- 2.8 Plotted is the numerical results for the nodal creep rate along the crack edge assuming a nonlinear ($n=3$) creep constitutive model. The values for the opening rate approximation and numerical results are read on the left vertical axis. This plot shows how the opening rate approximation varies from the numerical results as a function of the distance from the crack center. Also plotted is the percent error evaluated at each node. It is calculated as $\%Error = \frac{\dot{u}^{Nye} - \dot{u}^{comp}}{\dot{u}^{Nye}} * 100\%$, where \dot{u}^{Nye} is the analytical Nye solution eq. (2.2) and \dot{u}^{comp} are the numerical results for each node. For the value of the percent error please read the right vertical axis. 23
- 3.1 Sketch illustrating early October 2006 Synthetic Aperture Radar (SAR) image overlaid with the NASA Moderate Resolution Imaging Spectroradiometer (MODIS) image, showing the lake extent (blue) on 29 July 2006. This figure was redrawn here to approximately duplicate the features in Das et al. [10]. A GPS station measuring the ice displacement was located $\sim 1/4$ km from the lake shore. Hobo instruments located on the lakebed measured fluid pressure, from which lake depth versus time was inferred. . . 32

3.2	Data from the 2006 lake drainage event reproduced from Das et al. [10] with additional labeling by the authors: Lake level vs. time shown, as inferred from water-pressure loggers (Fig. 3.1) Hobo1 and Hobo2 (blue and magenta symbols and gray line, referred to right vertical axis; the dashed gray line is a linear fit to the last two lake-level measurements before loggers were left dry, suggesting that the lake drained completely prior to 17:30 UTC). Uplift at GPS site (Fig. 3.1), acquired with 5-min temporal resolution (black line, referred to left vertical axis; red line shows rate of uplift).	34
3.3	Schematic of subglacial drainage system showing the vertical influx $Q_{vert}(t)$ from the lake through the crack-crevasse system feeder channel, and the resulting water injection along the ice-bed interface. The feeder channel horizontal opening $\Delta\bar{u}$ includes contributions from elastic opening, $\Delta\bar{u}^{el}$, linearly proportional to the current fluid pressure, and prior creep opening, $\Delta\bar{u}^{cr}$, which accumulated over an extended time before the rapid drainage. The ice sheet height H is much larger than the lake depth and the basal fracture opening $h(x, t)$. Additionally, the lake diameter is also significantly smaller than the ultimate horizontal spread of $2L(t)$ of the basal hydraulic fracture.	35
3.4	Dependence of flow rate on inlet pressure for several values of the creep parameter C . In the model, the flow begins at $p_{inlet} = \rho g H$ (hydrostatic pressure), but then the pressure drops as flow rate develops, until the pressure p_{inlet} falls to the ice overburden pressure $\rho_{ice} g H$	45

3.5	A plot showing how the basal fracture length, inlet pressure, conduit opening, and water flux into the basal fracture evolve for a range of values of C between 0 and 2.0. Dots at the ends of the curves mark complete drainage of the lake. These results were produced using the parameters given in Tab. 3.1. We see that the flux into the fracture increases with C , leading to more rapid growth of the basal fracture. The average flux of $8700 \text{ m}^3/\text{s}$ inferred in [10] is plotted as a dashed line. Our results also show that inlet pressures quickly fall from the initial hydrostatic value to close to σ_o and this is accompanied by elastic closing of the conduit opening.	56
3.6	Data from the 2006 lake drainage event reproduced from Das et al. [10] with an additional curve showing our model prediction for the parameters given in Tab. 3.1 and $C = 2.0$, meaning that the creep opening is twice what would be the initial elastic opening of the crack-crevasse system if subjected to hydrostatic water pressure.	57
4.1	Physical space and boundary conditions for in-plane and antiplane motion around a channel: (a) dimensional and (b) nondimensional.	65

4.2	Horizontal antiplane strain rate $\partial U_z/\partial X$ (corresponding to dimensional $\dot{\gamma}_{xz}$) for $S \ll 1$, small antiplane perturbation of in-plane flow field: (a) analytical solution from for $\partial U_z/\partial X$, derivative of equation (4.13) and (b) the derivative of the numerical solution to equation (4.12), i.e. the nondimensional numerical strain rate $\dot{\Gamma}_{xz}^N$. The maximum value of horizontal strain rate, the strain rate concentration factor, $\xi_x = 3.7472\dots$ is located on the top of the channel. Black lines are drawn to denote the outer and inner edges of the domain in both figures.	74
4.3	Horizontal strain rate concentration factor $\xi_x = \dot{\gamma}_{xz}/\dot{\gamma}_{far}$ as a function of the antiplane to in-plane strain rate ratio $S (= \dot{\gamma}_{far}/A\Delta p^n)$ for a finite domain with outer radius $B = 10$. This value is the maximum strain rate in the domain and occurs along the Y -axis on the top of the channel, i.e. at $(0, a)$. For small values of S , ξ_x is given by the perturbation solution. For large S , we see that ξ_x approaches the fully antiplane value $\xi_x \approx 3.0768$ for the finite domain.	78
4.4	Numerical simulation results for the maximum effective strain rate and components \dot{E}_{rr} and $\xi_x/2$ as a function of S and evaluated at the top of the channel. The in-plane strain rate $\dot{E}_{rr} = \partial U_r/\partial R$ dominates for small S . The large S limit is given by the horizontal strain rate concentration factor $\xi_x = \partial U_z/\partial X$. The outer radius for these simulations is $B = 10$	80

4.5	Small antiplane perturbations in an “infinite” domain: (a) antiplane velocity U_z , comparing the perturbation solution $U_z(R; B)$ equation (4.13), solid line, and numerical solution (circle line) for U_z as a function of R along $\theta = 0$ with $B = 500$, $n = 3$, and $S = 10^{-3}$. Perturbation solution fit to simulation, equation (4.20), $U_z(R; \mathcal{R})$, dotted line, and outer solution for large R , equation (4.19), $U_z = R$, dashed line, are also plotted. (b) Transition radius \mathcal{R} , as computed by the fit $U_z(R; \mathcal{R})$ in (a), called $\mathcal{R}(S; \text{fit})$, as a function of S (circle line). Simple scaling, equation (4.18), $\mathcal{R} \sim 1/\sqrt{S}$, dashed line, and regime of validity outer domain size, equation (4.14), $B_{cr}(S)$ with $n = 3$, dotted line.	82
4.6	Average creep closure (radial velocity) $-\bar{U}_r$ as a function of R . The range of S is from $S = 10^{-5}$ (bottom circle line) to $S = 10^3$ (top circle line) in powers of ten. For all values of S , the average creep closure decays as $1/R$ (solid line). For small S , the creep closure asymptotes to the Nye solution. The outer radius for these simulations is $B = 10$.	87
4.7	Average creep closure (radial velocity) $-\bar{U}_r$ at $R = 1$ scaling for large S . The outer radius for these simulations is $B = 10$.	89
4.8	Röthlisberger channel diameter as a function of the antiplane to in-plane strain rate ratio S . The finite domain effects are scaled out. Representative ranges of S for ice streams and mountain glaciers are based on parameters from section 4.3.1 and table 4.1.	95

A.1	Uniaxial far-field stress applied in the y-direction. Respective stress concentration factor is given at the given locations of the ellipse. Because of symmetry, the stress concentration factors also applies to the other side of the ellipse along the same axis.	108
A.2	Uniaxial far-field stress applied in the x-direction. Respective stress concentration factor is given at the given locations of the ellipse. Because of symmetry, the stress concentration factors also applies to the other side of the ellipse along the same axis.	109
A.3	Stress concentration factors solution for hydrostatic tension can be achieved by the superposition of solution in fig. A.1 and fig. A.2. The superposition principle can only be used for a problem using a linear constitutive model, such as a linear creep material.	110
B.1	Root mean square of deviations of \dot{E}_{rr} from mean strain rate $\dot{\bar{E}}_{rr}$ as a function of R for all S . The range of S is from $S = 10^{-5}$ (bottom circle line) to $S = 10^3$ (top circle line) in powers of ten. The outer radius of the domain is $B = 10$.	115

Acknowledgments

I WOULD LIKE TO EXPRESS MY SCINCERE GRATITUDE TO Professor James R. Rice for providing me with guidance and support through every step of the research presented in this thesis, without whom this would have not been possible. I am grateful to Professor Katia Bertoldi for insightful discussions and for evaluating this thesis. I would like to also thank the generous financial support from the Harvard University School of Engineering and Applied Sciences Blue Hills Hydrology Endowment without which this would have not been possible. I take this opportunity to also thank the entire faculty of the Harvard School of Engineering and Applied Sciences for providing classes that have expanded my knowledge and enabled me to conduct the research presented in this thesis. I am also grateful to my partner Alaina who supported me and encouraged me through every step of this venture. I also thank my parents, Dula and Lora, and family for the unceasing encouragement, support and attention. Lastly, I would also like to thank my group members and office mates Thibaut, Colin, Farhad and John for insightful discussions and moral support.

1

Introduction

1.1 STRUCTURE OF THESIS

This thesis is broken down into two main parts that are distinctively related to the study of the dynamics of subglacial channels. The first part focuses on quantifying the creep opening of a crack-like crevasse under a supraglacial lake. For the second part of the thesis, I worked on numer-

ically quantifying the opening of a Röthlisberger channel in ice-stream shear margins, where antiplane shear stresses act in the perpendicular direction of the typical in-plane Röthlisberger solution. The thesis is organized in three main chapters (2-4) where chapter 2 and chapter 3 are papers on the supraglacial crack-crevasse work and chapter 4 is a paper on the Röthlisberger channel analysis. Lastly, chapter 5 is a conclusion stating the contributions to the field, and possible further extensions of the projects. Appendix A and Appendix B serve as more detailed or alternate derivations for specific quantities mentioned in chapter 2 and chapter 4, respectively.

1.2 SUPRAGLACIAL CRACK-CREVASSE

Data acquired from the western margin of the Greenland Ice sheet have shown that large supraglacial lakes, formed from snow and ice melt-water accumulation, are frequently able to form pathways connecting the lake's water to the bottom of the ice sheet. Once a connection has been made, the lake's water (with volume prior to rapid drainage of $\sim 44 \times 10^6 \text{ m}^3$) has been witnessed to drain fully in less than 2 hours. This rapid drainage ultimately enhances basal sliding, allowing the ice in the western margin of Greenland to flow faster. The process through which such pathways are created has been observed to be large crack crevasse systems, where the creep of ice plays a major role on the opening of the channel as explained in chapter 2 and chapter 3. Chapter 2

describes the opening of a crack in a power law creep material (where ice behaves as a power law creep material with creep exponent $n = 3$) under hydrostatic stress and chapter 3 discusses the implication of such crack opening in the supraglacial lake channel setting.

1.3 RÖTHLISBERGER CHANNEL WITH ANTI-PLANE SHEAR

In the West Antarctic Ice Sheet, specifically in the Siple Coast, ice streams are found as a principal drainage route for most of the ice mass loss throughout the year. In the ice streams' margins, where moving ice is separated from stagnant ice along the ridges, localized shear stresses cause a zone of heavily crevassed ice with concentrated deformation. In this zone Perol and Rice [30] have conjectured that water, created from shear heating of the ice, potentially drain through Röthlisberger channels that run along these shear margins. However, these channels are typically modeled as a 2 dimensional model and does not account for stresses in the perpendicular to the plane direction. Thus, chapter 4 describes how the Röthlisberger channel model is affected by superimposing an antiplane shear stress, directed perpendicular to the 2 dimensional plane strain model.

This work was a collaboration with Professor James R. Rice. I was the lead researcher on this project and primary author of the manuscript. My contribution to this project was to use numerical simulations to verify how the approximation differs from the numerical solution. For this project I created a Finite Element Method model of a crack in a power law creep material. The work in this section has not yet been published in an academic journal.

Fernandes, M.C. and Rice, J.R. (2015, *In prep.*).
Solution for the average opening of a crack in a
power-law creeping solid. Intended for
submission at the *International Journal of*
Fracture.

2

Solution for the average opening of a crack in a power-law creeping solid

2.1 ABSTRACT

In this paper, we use a combination of theories developed by Inglis, Kolosov and Eshelby to approximate the opening profile of a crack in an infinite power law creep material undergoing a far field hydrostatic tension. We use the Nye result for the opening of a circular channel in a power law creep material to get the magnitude of the radial opening of an arbitrary cavity, and use it in conjunction to the opening profile approximation to derive an approximation for the opening of a crack. However, this approximation is fully valid for a linear creep material (creep exponent $n = 1$) and for a circular cavity in a nonlinear creep material ($n \neq 1$). Then, we integrate the approximation for the opening to obtain an average opening rate. This expression is then corrected by introducing a correction factor that is obtained using a Finite Element Method model. Furthermore, the numerical model is validated using

two separate analytical expressions. Results portrayed in this paper are specifically for a power law creep material of $n = 3$ with application to the deformation of ice under a supraglacial lake, where a crack-crevasse system opens via creep connecting the lake's water to the bottom of the ice sheet.

2.2 INTRODUCTION

The ability to quantify the total opening of a crack in a power law creeping material is of fundamental importance when estimating fluid flow rate through a crack shaped conduit. Ice, which at long timescales is modeled as power law creeping solid, is of particular interest in this study and is motivated by the understanding a supraglacial lake (large body of water formed on the top surface of a glacier as a result of snow and ice melt-water accumulation) drainage event where the lake's water penetrated a 1 km thick ice sheet through a crack shaped conduit [10]. The present study arose because in order to model the lake drainage, we require to know how fast such crack conduit would open by creep when the crack surface is hydrostatically pressurized by the water. Although existing literature address the opening fields near the crack tip [22, 32] as well as quantify plastic fields resulting from stress singularities [21, 42], we contribute in estimating the steady state opening rate across the entire crack in a power-law creeping material. To address this issue we develop a simple approximation for the opening rate of the

crack and integrate it to find its total average opening. We correct the average opening approximation by introducing a correction factor, obtained from a Finite Element Method (FEM) model, that solely depends on the material creep exponent. Using this corrected opening approximation we are then able to compute the creep contribution to the total opening of a conduit under a supraglacial lake.

In order to simplify the problem, we begin by treating the crack as a 2 dimensional ellipsoidal cavity of major horizontal radius a and minor vertical radius b . Where if $a = b$ the cavity becomes circular and in the limit of $b/a \rightarrow 0$ the cavity becomes a crack (as illustrated in fig. 2.1). We apply a hydrostatic tensile stress denoted by σ_{appl} as a far-field boundary condition, which is equivalent to a hydrostatic pressure applied inside the cavity given that the material is incompressible. By applying the boundary condition on the far-field we are able to define the cavity surface as a traction free boundary.

Using Eshelby's result [14] of a cavity in a linear elastic material deforming homogeneously under hydrostatic stresses, we note that the stresses, strains, and displacement gradient must also retain homogeneity along its boundary. Likewise, this idea can be directly translated to the deformation of a cavity inside a linear creeping material, namely where the strain rates relate to the stresses through the rheology as $\dot{\epsilon}_E = A\tau_E^n$ with $n = 1$. Here, A describes the material creep compliance and the subscript E denotes the second invariant of the tensor which

will be described in more detail in the upcoming section.

As a result of the homogeneous opening rate within the cavity, the opening of any ellipsoidal shape cavity inside a linear creeping material will scale with the position within the boundary, namely $u_y \sim y$. Furthermore, since we know that y along the boundary of an ellipse is given by $y = \frac{b}{a}\sqrt{a^2 - x^2}$, then an expression for the y -opening of a cavity will simply be

$$\dot{u}_y = \frac{\mathcal{C}}{a}\sqrt{a^2 - x^2}, \quad (2.1)$$

where \mathcal{C} is a magnitude determined by the creep opening in the radial direction. Note that this expression is independent of the minor axis b , which we can set to $b = 0$ making this a valid expression for the opening rate of a crack. However, this only works for the linear case because it is known that the radial opening rate is uniform. For a non-linear creeping material, namely when $n \neq 1$, the solution will only be uniform when the cavity is circular. In other words, eq. (2.1) only works when $a = b$ for $n \neq 1$. This is the case for the material property of ice as defined by Glenn's law [19] to have a creep exponent of $n = 3$.

To obtain the radial opening of a circular cavity we use Nye's 1953 [29] result describing the opening rate of a circular channel in an infinite power law creep material. The result, which is valid for a circular cavity in a power law creep material of arbitrary creep exponent n , is given by

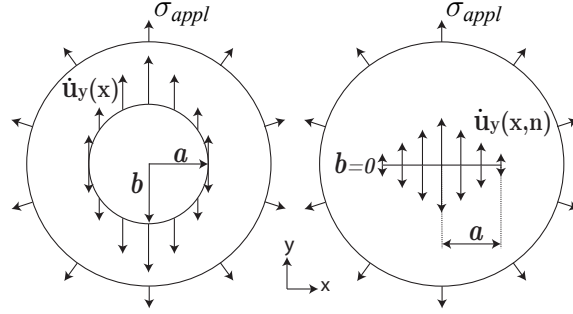


Figure 2.1: Figure illustrates the non-dimensional y-opening rate of a circular shape cavity and of a crack shaped cavity within an infinite power law creep medium. The cavity, in the infinite medium undergoes a net hydrostatic tension applied as a far-field boundary condition. The y-opening rate of both, a circular cavity and a crack, are dependent on the x position from the center of the cavity.

the expressions

$$\dot{u}_r(r) = A \frac{a^2}{r} \left(\frac{\sigma_{appl}}{n} \right)^n, \quad \dot{u}_\theta = 0, \quad (2.2)$$

where a is the radius of the channel, r is the distance from the center of the channel, and σ_{appl} is the pressure inside of the channel, which is equivalent to applying it as a far-field tensile stress. Furthermore, evaluating the Nye solution (2.2) at $r = a$ gives us the opening rate along the cavity boundary. Combining eq. (2.1) and eq. (2.2) at $r = a$ we obtain an expression for the y-opening rate of the cavity as (see Appendix A.2 for more detailed derivation)

$$\dot{u}_y = A \left(\frac{\sigma_{appl}}{n} \right)^n \sqrt{a^2 - x^2}. \quad (2.3)$$

Hereafter we will refer to eq. (2.3) as the opening rate approximation

and use upper case letters for nondimensional variables and lower case letters for dimensional variables. We can now nondimensionalize the opening rate in eq. (2.3) by Nye's solution (eq. (2.2)) as $\dot{u}_y = Aa \left(\frac{\sigma_{appl}}{n}\right)^n \dot{U}_y$ and nondimensionalize x by the channel radius $x = aX$. Therefore, the nondimensional opening rate approximation becomes

$$\dot{U}_y = \sqrt{1 - X^2}. \quad (2.4)$$

Note that this expression is the same as introduced by Inglis-Kolosov [23, 25] in 1913-1914 for the opening of a crack in a linear elastic medium. Here, we obtain the average opening rate by averaging the dimensional opening rate approximation eq. (2.3) along the cavity boundary such that

$$\bar{\dot{u}}_y = \frac{1}{a} \int_0^a \dot{u}_y dx. \quad (2.5)$$

Nondimensionally, we can evaluate the integral by using eq. (2.4) as

$$\bar{\dot{U}}_y = \int_0^1 \dot{U}_y dX = \frac{\pi}{4} \quad (2.6)$$

where $\bar{\dot{u}}_y = Aa \left(\frac{\sigma_{appl}}{n}\right)^n \bar{\dot{U}}_y$. Since it is known that the opening area of a crack in a nonlinear power law medium ($n \neq 1$) is going to differ from the solution given by eq. (2.5), the average opening rate of a crack-like cavity incised in ice can be corrected by introducing a numerical correc-

tion factor $\kappa(n)$

$$\bar{U}_y^{crack} = \bar{U}_y \kappa(n). \quad (2.7)$$

In the following sections we construct a FEM model that provides values for $\kappa(3)$ quantifying the average opening rate of a glacial vertical crack-crevasse.

2.3 NUMERICAL MODEL DESCRIPTION

2.3.1 CONSTITUTIVE MODEL

A commercial FEM package, *ABAQUS 6.12-1*, was used for the numerical part of this paper. The constitutive model used is a power-law creep material described by $\dot{\epsilon}_E = A\tau_E^n$, where $\dot{\epsilon}_E = \sqrt{\frac{1}{2}\dot{\epsilon}_{ij}\dot{\epsilon}_{ij}}$ is the equivalent shear strain rate and $\tau_E = \sqrt{\frac{1}{2}s_{ij}s_{ij}}$ is the equivalent shear stress (with $s_{ij} = \sigma_{ij} - \delta_{ij}\frac{\sigma_{kk}}{3}$ being the deviatoric stress tensor). Furthermore, the constitutive model assumes incompressibility in the form $\delta_{ij}\dot{\epsilon}_{ij} = 0$ (where δ_{ij} is the Kronecker delta). The numerical model is formulated as a Maxwell model (the strain is modeled as elastic and viscous elements in series), so that when solved within small geometry change assumptions, the displacement rates converge to those of a purely viscous material. Therefore, the model is allowed to respond to suddenly applied and sustained boundary loading, but on a timescale before the crack has opened enough to respond differently from a straight cut.

2.3.2 GEOMETRIC DOMAIN DESCRIPTION

The discretized numerical domain of the model is constructed as a quarter circular shape with a cavity (circular or crack shaped) located at its center. The ratio between the outer radius of the domain over the crack length is optimized to avoid generating results portraying a finite domain. This is done by varying the outer domain diameter until it is large enough where changes become negligible along the face of the crack. In addition, the cavity opening rate is corrected by introducing a correction factor based on the Nye solution for a finite domain (see Appendix A.1). This correction factor is implemented through the rheology coefficient A by making the material stiffer ultimately accounting for finiteness of the outer boundary.

2.3.3 BOUNDARY CONDITIONS

A tensile opening pressure, equivalent to that of the difference between the fluid pressure p_w and the ice overburden stress σ_o (stress caused by the mass weight of the ice) $\sigma_{appl} = p_w - \sigma_o$, is exerted along the outer edge of the domain. Given the quarter symmetry of the problem, we are able to analyze one quadrant of the domain and apply symmetry conditions (surface normal displacements constrained to zero) along the symmetry cuts within the model.

2.3.4 FEM MODEL MESHING

Fig. 2.2 shows the domain mesh discretized using 8-noded bi-quadratic plane strain elements with reduced integration (*ABAQUS* element code CPE8R)[11]. In order to accurately obtain results for stress, strain and displacements near the crack tip singularity, we model the crack tip as a collapsed ring of quadrilateral elements. This meshing method provides accurate results for a $1/r$ type singularity. However, because of the power-law hardening material model, we expect the singularity to behave as $r^{\frac{-1}{n+1}}$. Therefore, we numerically treat the singularity as a combination of $1/r$ and square root singularities by using the quarter point method in addition to the described meshing layout. This method entails moving the mid-side nodes on the sides connected to the crack tip to the $1/4$ point nearest the crack tip [26].

2.4 NUMERICAL VALIDATION

2.4.1 FULLY CREEP REGIME

In order to overcome the model's elastic relaxation, to the extent that the fully plastic creep regime is obtained, we allow the model to run long enough until the average opening creep rate ($\bar{\dot{U}}_y$) converges to a steady state solution. We derive a timescale t_R for the elastic relaxation time by

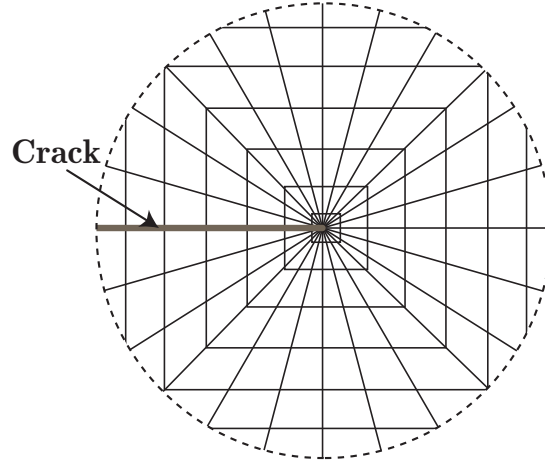


Figure 2.2: Zoomed in figure of FEM discretization near the crack tip, where the crack face is highlighted as the horizontal gray line. A quarter point method is used for the node placement near the crack tip to capture the square root singularity, and the crack tip is modeled as a collapse ring of quadrilateral elements to capture the $1/r$ singularity.

using Maxwell's model such that

$$\frac{d\epsilon}{dt} = \frac{1}{E} \frac{\partial \sigma}{\partial t} + \sigma^n A \Rightarrow t_R \sim \frac{1}{EA\sigma^{n-1}}. \quad (2.8)$$

2.4.2 VALIDATING MODEL USING NYE SOLUTION

In this section, we quantify the numerical error of the FEM model by comparing it's results to the opening rate approximation eq. (2.3), which in a linear creeping rheology ($n = 1$) it is known to exact solution. In nondimensional form, the becomes $\dot{U}_y = \sqrt{1 - X^2}$ as described by eq. (2.4). This analytical opening is compared to the opening rate obtained from the nondimensional FEM model in fig. 2.4. The close agreement

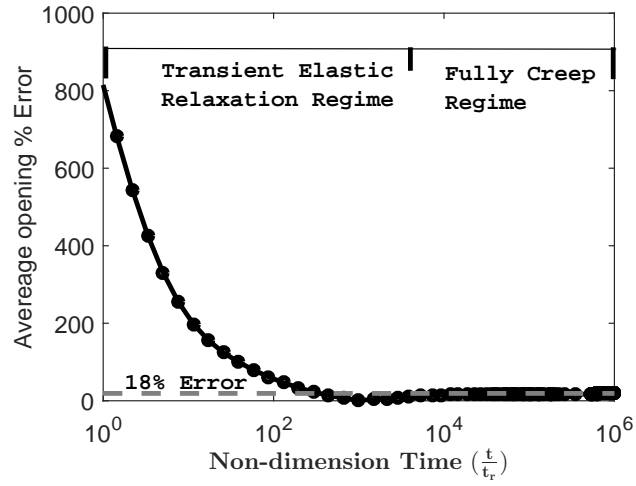


Figure 2.3: This plot validates the steady state fully plastic creep regime of the model. The simulation time is nondimensionalized using the timescale described in eq. (2.8). The velocity is nondimensionalized using the known Nye solution for the circular channel. In this semi-log plot, it is apparent that the time required for the elastic relaxation to have negligible impact on the steady state solution is around $10^3 * t_R$

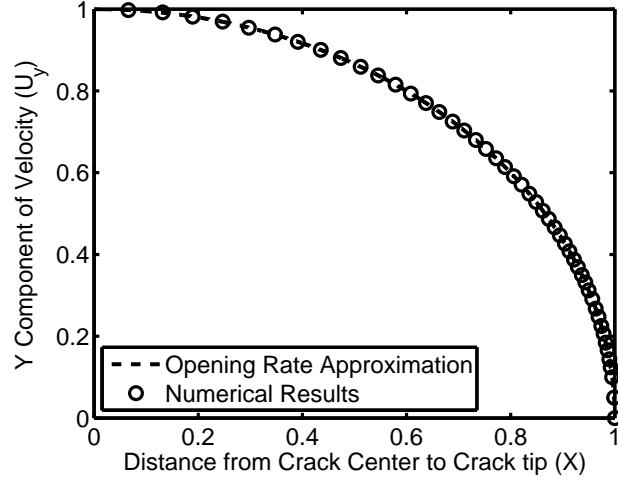


Figure 2.4: Benchmark of numerical model to analytic solution. This figure shows the numerical results overlaid on the Nye analytic solution for a crack under linear creep material model. The numerical results closely contour the analytic solution conveying little to no error.

between the numerical results and analytical expression suggests that the model meshing appropriately accounts for the square root singularity near the crack tip as well as for the far field crack opening behavior. Furthermore, using these results we benchmark the model's accuracy by analyzing the nodal percent error distribution along the crack edge as shown in fig. 2.5. Although, the percent error increases near the crack tip, the numerical model remains within 0.1 percent of the benchmark solution. By integrating the error over the crack face and dividing it by the length, analogous to the method for evaluating the average opening rate of eq. (2.5), we get that the average numerical error for the FEM model is $\sim 0.03\%$.

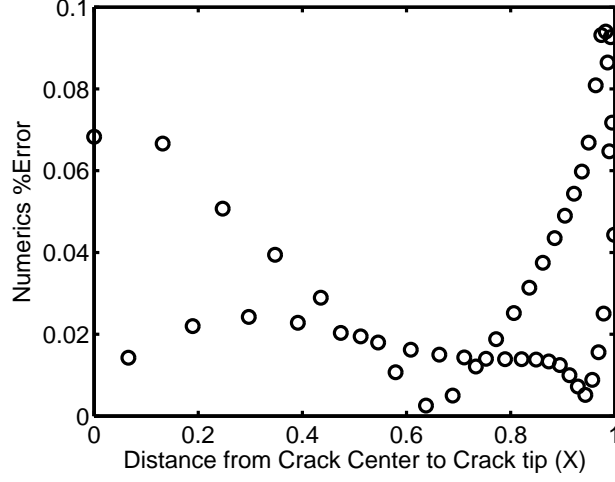


Figure 2.5: Error analysis comparing numerical simulation to known analytic solution. This figure shows the percent error calculated as $\%Error = \frac{u^{Nye} - u^{comp}}{u^{Nye}} * 100\%$, where u^{Nye} is the analytical Nye solution eq. (2.2) and u^{comp} are the numerical results for each node seen in fig. 2.4.

2.4.3 VALIDATING MODEL USING HRR FIELD

Here we use a different analytical expression to check the model's accuracy in obtaining the singularity fields near the crack tip of a nonlinear power law creep material. The HRR field, as described by Hutchinson, Rice and Rosengren [22, 32], is a field valid near the crack tip given by

$$\sigma_{ij} \rightarrow r^{-N/(1+N)} \Sigma_{ij}(\theta) \quad (2.9)$$

$$\epsilon_{ij} \rightarrow r^{-1/(1+N)} E_{ij}(\theta) \text{ where } N = \frac{1}{n} \quad (2.10)$$

for stresses and strains, respectively. Using simple constitutive laws, the HRR scaling for the creep opening rate is

$$\dot{u}_i(r, \theta) = r \left(\frac{1}{r} \right)^{n/n+1} h_i(\theta, n), \text{ where } \dot{\varepsilon} = A\tau^n. \quad (2.11)$$

For Glenn's law, where the creep exponent is defined as $n = 3$, this means that the HRR opening is described by

$$\dot{u}_i(r, \theta) = r^{1/4} h_i(\theta, n = 3). \quad (2.12)$$

When evaluated along the crack edge (where θ is constant) we eliminate the dependence on θ , thus resulting on the opening rate scaling of

$$\dot{u}_y(r) = \eta r^{1/4}. \quad (2.13)$$

Where η is a unknown constant that can be determined by fitting the numerical results near the crack tip. The comparison between the numerical results and the scaled analytic solution can be found in fig. 2.6. Although this result does not yield a quantitative error comparison, it does provide insight on the adequacy of the mesh near the crack tip for a combination of $1/r$ and square root singularities.

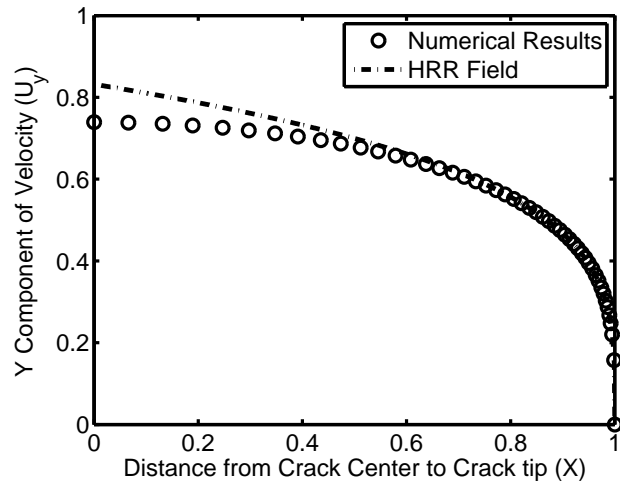


Figure 2.6: This is a benchmark for the numerical results assuming a non-linear power law rheology. The near crack tip region closely contours the numerical results attained from the simulation. This proves that the mesh in the crack tip region is adequately constructed. In the region away from the crack tip singularity (more than $\sim 20\%$ of crack length away from the tip), the HRR solution does not accurately describe the stress and strain fields, thus it cannot serve as a benchmark for the model in that region.

2.5 EXPLORING THE DOUBLE HRR OPENING SOLUTION

For a linear material ($n = 1$) we know that the nondimensional solution for the opening scales as

$$\sim \sqrt{1 - X^2} \quad (2.14)$$

where we can separate this into two roots, namely

$$\sqrt{1 - X}\sqrt{1 + X}. \quad (2.15)$$

Using this logic, we can approximate the opening of a nonlinear creep material by using a double HRR field

$$\dot{u}_y = \zeta(n)(1 - X)^{1/n+1}(1 + X)^{1/n+1} \quad (2.16)$$

where $\zeta(n)$ is an unknown constant which is determined by fitting the numerical data. Thus for $n = 3$ we get that the opening is described by

$$\dot{u}_y = \zeta(3)(1 - X)^{1/4}(1 + X)^{1/4}. \quad (2.17)$$

The idea of the double HRR field is based on having the crack tip field of one side affect the crack tip field of the other side. Thus, if we compare the double HRR field to the numerical result, as shown in fig. 2.7, we see that it does a much better job approximating the opening rate of a crack

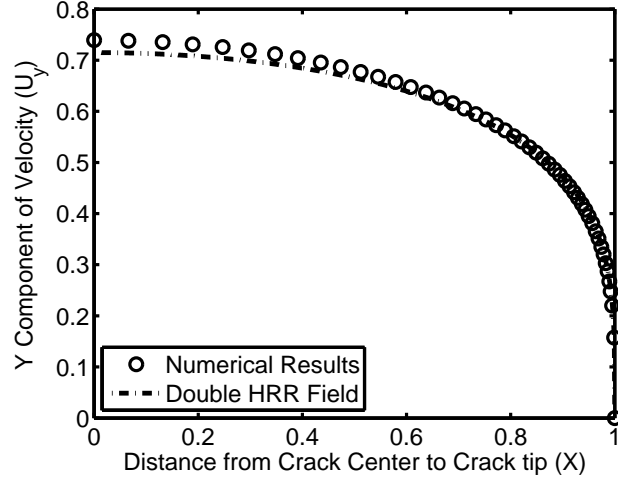


Figure 2.7: Plotted is the nondimensional double HRR solution for the opening of a crack in a power law creep material with $n = 3$ (eq. (2.17)) as compared to the nondimensional numerical simulation for $n = 3$.

in a nonlinear creep material than eq. (2.4). The results presented in this section are preliminary and will be further explored for adequacy on portraying the opening profile of a cavity in an arbitrary power law creeping material.

2.6 RESULTS

After benchmarking the numerics against known analytic solutions, we can confidently quantify how well the opening rate approximation holds for a crack like geometry in a $n = 3$ power law creep material such as ice. Figure 2.8 shows the opening rate approximation overlapped with the numerical results (dashed graph and open circles, respectively).

From this figure, it is apparent that the power law material has an overall slower creep velocity than the approximation describes. The percent error plot, portrayed by the bold asterisks using right axis of Figure 2.8, shows that away from the crack tip the approximation overshoots the solution by $\sim 25\%$. As it approaches the crack tip, namely 80% of the way to the crack tip, the approximation begins to undershoot and very near the crack tip the approximation undershoots almost 220% of the opening numerical solution. Although the error near the crack tip may seem large, the contribution to the total average opening is negligible. Thus, the main contribution to the total average opening rate is along the overshoot regime of the approximation, namely when $X < 0.8$. In order to get an overall error estimate, we integrate the numerical solution to achieve the average y-opening rate \bar{U}_y numerically, as described by eq. (2.6). Comparing that to the average opening rate approximation of $\pi/4$, we can compute the correction factor $\kappa(3)$ necessary to allow this approximation to work. This yields an average opening velocity correction factor for the approximation of $\kappa(n = 3) = 0.811$. In other words, the dimensional approximation for the average opening rate of the crack like cavity (taking into account both the opening of both sides of the crack) in a power law creep material where $n = 3$ can be described by

$$\bar{u}_y = (0.8111) \left(\frac{\pi}{2} \right) Aa \left(\frac{\sigma_{appl}}{3} \right)^3. \quad (2.18)$$

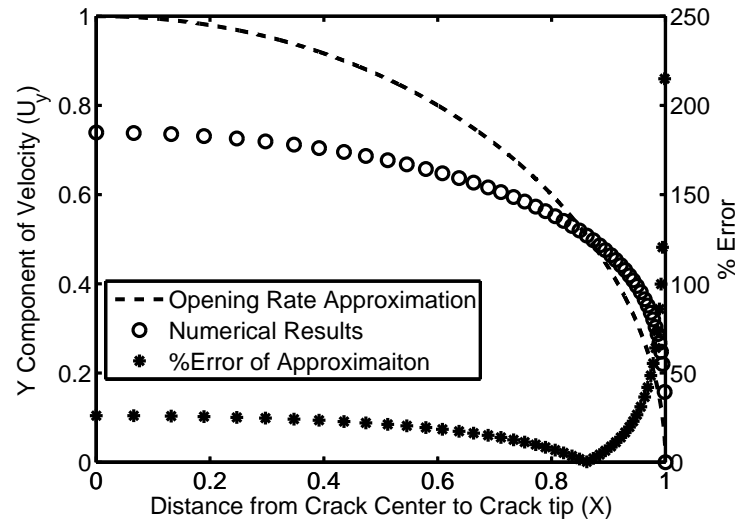


Figure 2.8: Plotted is the numerical results for the nodal creep rate along the crack edge assuming a nonlinear ($n=3$) creep constitutive model. The values for the opening rate approximation and numerical results are read on the left vertical axis. This plot shows how the opening rate approximation varies from the numerical results as a function of the distance from the crack center. Also plotted is the percent error evaluated at each node. It is calculated as $\%Error = \frac{\dot{u}^{Nye} - \dot{u}^{comp}}{\dot{u}^{Nye}} * 100\%$, where \dot{u}^{Nye} is the analytical Nye solution eq. (2.2) and \dot{u}^{comp} are the numerical results for each node. For the value of the percent error please read the right vertical axis.

2.7 DISCUSSION

During summers, the collection of surface melt-water on the Greenland Ice Sheet leads to formation of massive lakes, known as supraglacial lakes, which can be as large as several square kilometers in area. Recent observations show that ice flow along the western margin accelerates during the summer when surface melt-water lubricates glacial sliding at the ice-bedrock interface [3]. Supraglacial lakes, often with a volume of $\sim 10^7 \text{ m}^3$, have enough water to fill 4000 Standard Olympic swimming pools and have been observed to fully drain within two hours [27]. These observations suggest that after an unsteady vertical hydraulic fracture through the ice, the water is able to flow turbulently ($Re \approx 10^5$) through the $\sim 1 \text{ km}$ thick sheet, eventually reaching the ice-bedrock interface. After the water reaches the bottom of the ice sheet, it flows horizontally outward into a thin layer, lifting up the ice and significantly enhancing basal sliding. Previous research conducted on the Greenland Ice Sheet by Das et al. [10] showed that water-driven fracture propagation from supraglacial lake drainage is correlated with increased seismic behavior, ice sheet uplift, transient acceleration, and subsequently the horizontal displacement of glaciers. Previous studies by Tsai and Rice [40] attempt to explain the remarkably short timescale of $\sim 2 \text{ hrs}$ for the lake's full drainage. Although the study yielded order-of-magnitude agreement with the drainage data from Das et al. [10], the

study is improved in this paper by accounting for the creep opening of the vertical crevasse.

Therefore, to more accurately estimate the total opening of the crack-crevasse channel under a supraglacial lake, we divide the total average opening of the crack into separate elastic and creep parts such that the total average opening at a specified time is given by $\Delta\bar{u}(t) = \Delta\bar{u}^{el} + \Delta\bar{u}^{cr}(t)$. Furthermore, we use Rice et. al's [34] scaling, describing the ratio of prior creep opening to elastic opening of the channel under hydrostatic pressure given as

$$C = (\Delta\bar{u}^{cr}|_{p=p_{hydrst}}) / (\Delta\bar{u}^{el}|_{p=p_{hydrst}}), \quad (2.19)$$

where $p_{hydrst} = (\rho_w - \rho_i)gH$ is the hydrostatic pressure, g is the gravitational acceleration, H is the ice sheet thickness, and ρ_w and ρ_i are the mass densities of water and ice, respectively. To get the average creep opening we integrate the creep rate over time, assuming it not to change significantly during the short time scale of the drainage, and obtain

$$\Delta\bar{u}^{cr}(t) = 2t\bar{\dot{u}}_y = At\alpha\kappa(3)\frac{\pi}{2}\left(\frac{\sigma_{appl}}{3}\right)^3, \quad (2.20)$$

where t is the time, and the factor of 2 comes from the crack opening along both faces. Similarly, the elastic opening for both sides of the crack is given from [34] as

$$\Delta\bar{u}^{el} = \frac{\pi a(\sigma_{appl})}{E'}, \quad (2.21)$$

where E' is the effective plane strain modulus ($E' = E/(1-\nu^2)$). Furthermore, for the problem of the pressurized crack-crevasse, we know that the stress imposed along the boundary of the crack will be $\sigma_{appl} = \frac{p_w - \sigma_o}{2}$, where $p_w = \rho_w g H$ is the hydrostatic water pressure, $\sigma_o = \rho_i g H$ is the ice overburden, and the factor of $\frac{1}{2}$ comes from averaging the pressure inside the channel across the thickness of the ice sheet (assuming a uniform pressure gradient). Using this defined value for σ_{appl} , eq. (2.19), eq. (2.20), and eq. (2.21) we obtain a time scaling given by

$$t = \frac{54}{0.8111} \frac{((\rho_w - \rho_i)gH/2)^{-2}}{AE'} \quad (2.22)$$

where A is the creep compliance parameter when $n = 3$.

2.8 CONCLUSION

Using a combination of Eshelby, Inglis, Kolosov and Nye's solution in addition to a numerical FEM model, we describe the average opening rate of a crack (accounting for the opening of both sides of the crack) in a nonlinear material as

$$\bar{\dot{u}}_y = Aa\kappa(n)\frac{\pi}{2}\left(\frac{\sigma_{appl}}{n}\right)^n, \quad (2.23)$$

commonly referenced in this paper as the opening rate approximation. Using an FEM model, we find that the correction factor $\kappa(n)$ for ice (where

$n = 3$) is $\kappa(3) = 0.811$. This solution describes the creep contribution to the total opening of a crack crevasse system below a supraglacial lake. Using the average creep opening solution in conjunction with the average elastic opening solution (eq. 2.21) and the scaling C , we derive the time scale for the total opening of the crevasse as described by eq. (2.22). Furthermore, the model can be expanded to different values of n , such that the correction factor $\kappa(n)$ is known and is currently in preparation.

This project was a collaboration with Professor James R. Rice, Professor Victor C. Tsai and Dr. John D. Platt. My role in this project was to create Finite Element Method model comparing the creep opening of the crevasse to the elastic opening of the crevasse. In this project I also created the code to look at the average temperature distribution across the ice sheet. This work has been published in the Journal of Applied Mechanics.

Rice, J.R., Tsai, V.C., Fernandes, M.C., and Platt, J.D.
(2015). Time Scale for Rapid Draining of a
Surficial Lake into the Greenland Ice Sheet.
Journal of Applied Mechanics.

3

Time Scale for Rapid Draining of a Surficial Lake into the Greenland Ice Sheet

3.1 ABSTRACT

A 2008 report by Das et al. documented the rapid drainage during summer 2006 of a supra-glacial lake, of approximately 44×10^6 cubic meters, into the Greenland Ice Sheet over a time scale moderately longer than 1 hour. The lake had been instrumented to record the time-dependent fall of water level, and the uplift of the ice nearby. Liquid water, denser than ice, was presumed to have descended through the sheet along a crevasse system, and spread along the bed as a hydraulic fracture. That event led two of the present authors to initiate modeling studies on such natural hydraulic fractures. Building on results of those studies, we attempt to better explain the time evolution of such a drainage event. We find that the estimated time has a strong dependence on how much a pre-existing crack/crevasse system, acting as a feeder channel to the bed, has opened by slow creep prior to the time at which a basal hy-

draulic fracture nucleates. We quantify the process and identify appropriate parameter ranges, particularly of the average temperature of the ice beneath the lake (important for the slow creep opening of the crevasse). We show that average ice temperatures 5 to 7°C below melting allow such rapid drainage on a time scale which agrees well with the 2006 observations.

3.2 INTRODUCTION

As annual late spring and summer temperatures affect the Greenland ice sheet, there is extensive meltwater generation and flow over its surface. Observations show that this water often collects in surficial lakes. A particular lake, located near the western margin of Greenland (68.72°N, 49.50°W), was instrumented during 2006 by Das et al. [10]; see Fig. 3.1 and Fig. 3.2 based on their work. It provided a remarkably clear record of the rapid disappearance of the lake's water into the ice. Our previous studies [1, 39, 40] supported quantitatively their [10] suggestion that the liquid had proceeded downward along a major crevasse system extending below the lake, through a process suggested by Weertman [46], and then propagated as a turbulently driven hydraulic fracture along the ice/rock interface at the base (see below).

The basic facts about the supraglacial meltwater lake are as follows [10] (Fig. 3.1 and Fig. 3.2):

1. The lake began filling in July 2006.

2. The lake surface level reached a maximum at $\sim 0:00$ hr on 29 July 2006.
3. At that maximum, the lake volume was $\sim 44 \times 10^6 \text{ m}^3$, and surface area $\sim 5.6 \text{ km}^2$.
4. Shortly after $\sim 0:00$ the level (marked by the “Falling lake level” curve in Fig. 3.2, and read on the right-side scale) was observed to slowly/steadily fall at $\sim 15 \text{ mm/hr}$.
5. The rate of fall became much more rapid shortly after 16:00 hr.
6. Then, within ~ 1.5 hr, the lakewater rapidly disappeared into the ice, with the lake surface falling at a maximum rate of $\sim 12 \text{ m/hr}$, with the maximum volumetric discharge rate $Q > 10,000 \text{ m}^3/\text{s}$, and average rate $Q \sim 8,700 \text{ m}^3/\text{s}$ during the discharge. (In comparison, for the Niagara River leading to Niagara Falls, the average Q is $\sim 5,750 \text{ m}^3/\text{s}$ [38]).

The lake level H_{Lake} during drainage was determined from two pressure meters (Hobo 1 and 2), see Fig. 3.1, although these were left dry (Fig. 3.2, curve denoted H_{Lake} , with axis scale on right side) well before full drainage. A GPS instrument was placed $\sim 0.7 \text{ km}$ from the lake edge, but yet further from the $\sim 2.7 \text{ km}$ long crevasse system (Fig. 3.1) through which the water is presumed to have drained. The uplift it recorded is labeled Z_{rel} , the black curve with axis scale on the left, and its time rate is shown in red. We have marked the 1.15 m maximum transient uplift Z_{rel} , attained at $\sim 17:40$ hr, whereas the uplift rate dZ_{rel}/dt is maximum at $\sim 17:00$ hr.

A simple calculation suggests that the water entering beneath the ice sheet, transiently lifting it from its bed, does so by a strongly turbulent

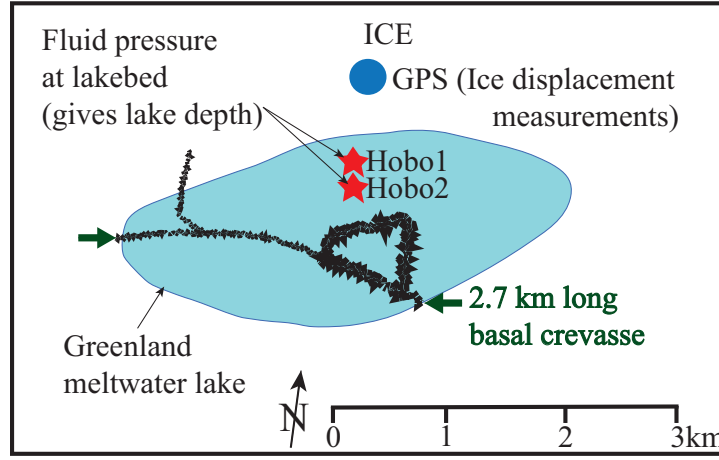


Figure 3.1: Sketch illustrating early October 2006 Synthetic Aperture Radar (SAR) image overlaid with the NASA Moderate Resolution Imaging Spectroradiometer (MODIS) image, showing the lake extent (blue) on 29 July 2006. This figure was redrawn here to approximately duplicate the features in Das et al. [10]. A GPS station measuring the ice displacement was located $\sim 1/4$ km from the lake shore. Hobo instruments located on the lakebed measured fluid pressure, from which lake depth versus time was inferred.

flow. Let R be the radius of the subglacial fracture, approximated for simplicity as circular, near the condition of full lake discharge. Then $\pi R^2 \times \text{uplift of } 1.15\text{m} \approx \text{the lake volume of } 44 \times 10^6 \text{ m}^3$, giving $R \approx 3.5$ km at full drainage. Since that takes about 1.2 hr to occur, the average fracture growth speed along the interface can be approximated as $R/1.2 \text{ hr} \approx 3 \text{ km/hr}$. Recalling that the kinematic viscosity of water is $\sim 10^{-6} \text{ m}^2/\text{s}$, the Reynolds number for flow in the fracture is

$$Re = (3\text{km/hr} \times 1.15\text{m}) / (10^{-6} \text{ m}^2/\text{s}) \approx 8 \times 10^5 \quad (3.1)$$

and numbers in excess of 10^5 would still be appropriate if we reduced

the assumed gap size significantly, as may be appropriate for the earlier phases of the fracture propagation.

However, although our initial attempt [40] to explain the remarkably short time scale for the lake disappearance yielded order-of-magnitude agreement, it did not agree precisely with observations. Ice, like all solids, responds elastically on short time scales, although creep deformation becomes dominant on longer time scales [8]. The assumption of elastic response seems appropriate over the short time scale of the lake drainage, of order 1.5 hrs in Fig. 3.1. Nevertheless, we argue here that a critical aspect of the drainage process was developing by creep flow, well before the onset of rapid drainage. That creep, a process to which Needleman and co-workers [6, 28] have contributed insightful computational methodology in other contexts, plays an important role in determining the estimated time scale of the lake drainage.

3.3 ANALYSIS

To model the drainage event, or at least a simple but tractable representation of it, we adopt the solution of [39] for an ice sheet of uniform thickness H (≈ 1 km), see Fig. 3.3, in which a vertical crevasse connected to the lake supplies water to a growing opening gap (basal fracture) along the bed, with fluid inlet pressure $p_{inlet}(t)$ at the entry point. The equation system solved in [39] generalized that in [40] to allow the

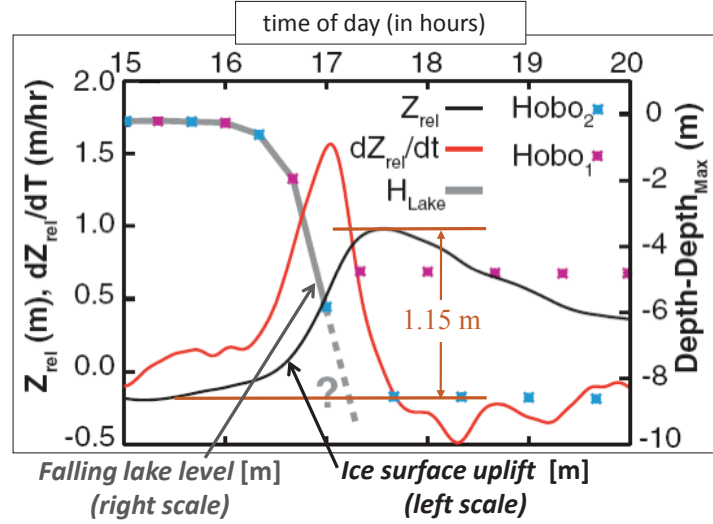


Figure 3.2: Data from the 2006 lake drainage event reproduced from Das et al. [10] with additional labeling by the authors: Lake level vs. time shown, as inferred from water-pressure loggers (Fig. 3.1) Hobo1 and Hobo2 (blue and magenta symbols and gray line, referred to right vertical axis; the dashed gray line is a linear fit to the last two lake-level measurements before loggers were left dry, suggesting that the lake drained completely prior to 17:30 UTC.). Uplift at GPS site (Fig. 3.1), acquired with 5-min temporal resolution (black line, referred to left vertical axis; red line shows rate of uplift).

crack half-length $L(t)$ to be comparable to and several times larger than ice thickness H (whereas [40] presented a self-similar solution for the range $L(t)/H \ll 1$, i.e., effectively for a fracture at the base of an unbounded domain).

The modeling of [39] assumes, as justified in retrospect, that for purposes of calculating the elastic deformation and hence the crack opening displacement, that only the local fluid pressure $p(x, t)$ [$= -\sigma_{zz}(x, z = 0, t)$] need be considered. That is because it is normally far greater than the shear tractions $\tau_{wall}(x, t)$ [$= -\sigma_{zx}(x, z = 0, t)$] exerted along the walls

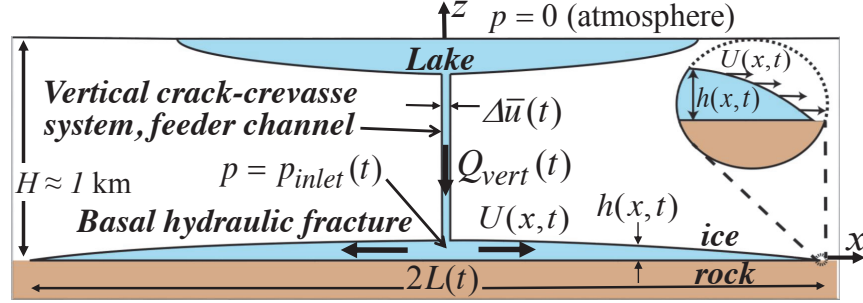


Figure 3.3: Schematic of subglacial drainage system showing the vertical influx $Q_{vert}(t)$ from the lake through the crack-crevasse system feeder channel, and the resulting water injection along the ice-bed interface. The feeder channel horizontal opening $\Delta\bar{u}$ includes contributions from elastic opening, $\Delta\bar{u}^{el}$, linearly proportional to the current fluid pressure, and prior creep opening, $\Delta\bar{u}^{cr}$, which accumulated over an extended time before the rapid drainage. The ice sheet height H is much larger than the lake depth and the basal fracture opening $h(x, t)$. Additionally, the lake diameter is also significantly smaller than the ultimate horizontal spread of $2L(t)$ of the basal hydraulic fracture.

of the fracture from resistance to fluid infiltration. To solve for the crack opening in a manner which solves the elasticity equations in 2D plane strain, and meets the traction-free surface boundary conditions at $z = H$, the numerical integral equation formulation of Erdogan et al. [13] (with correction of a mis-printed kernel as noted in [41]) was used. That relates the pressure distribution $p(x, t)$ to the crack opening gap $h(x, t)$ at each time t (with inertia neglected because of the slowness of fracture propagation speeds relative to elastic wave speeds). Also, in view of the low fracture toughness of ice, $K_{Ic} \approx 0.1$ MPa, it was judged that toughness became unimportant, in the sense quantified by Garagash and Detournay [17], once crack half-length $L(t)$ was greater than ≈ 10 m. Ef-

fectively, over the long length scale of fracture growth ($L > 1$ km), the problem of fracture becomes asymptotically indistinguishable from the problem of lift-off along a non-adhering (zero K_{lc}) interface.

Elasticity theory under plane strain conditions in the x - z plane, and within the usual approximations of linear elastic theory, relates displacement discontinuities $\Delta u_x(x, t)$ and $\Delta u_z(x, t)$ (along the fracture plane $z = 0$, between $x = -L(t)$ and $x = +L(t)$), to the traction stress components acting on that plane and in adjacent material by

$$\begin{aligned} \left\{ \begin{array}{c} \sigma_{zx}(x, z, t)/E' \\ \sigma_{zz}(x, z, t)/E' \end{array} \right\} = \\ \int_{-L(t)}^{+L(t)} \left(\begin{array}{cc} K_{xx}(x - x', z) & K_{xz}(x - x', z) \\ K_{zx}(x - x', z) & K_{zz}(x - x', z) \end{array} \right) \frac{\partial}{\partial x'} \left\{ \begin{array}{c} \Delta u_x(x', t) \\ \Delta u_z(x', t) \end{array} \right\} dx'. \end{aligned} \quad (3.2)$$

The notation here is that, with $u_\alpha = u_\alpha(x, z, t)$, for $\alpha = x$ or z , $\Delta u_\alpha(x, t) = u_\alpha(x, z = 0^+, t) - u_\alpha(x, z = 0^-, t)$. The kernels K_{xx} , K_{xz} , K_{zx} , and K_{zz} all vanish on the plane $z = H$, the surface of the ice sheet, so as to meet the traction-free boundary condition. Also, on the plane $z = 0$, the diagonal kernels K_{xx} and K_{zz} include terms which are Cauchy singular, like $1/(x - x')$. Here $E' = E/(1 - \nu^2)$ where E is Young's modulus and ν is the Poisson ratio. The full form of the kernels as $z \rightarrow 0^+$, the upper side of the fracture plane (i.e., the base of the ice sheet), is given by Erdogan et al. [13], although a misprint as identified in [41] must be corrected.

As $z \rightarrow 0^+$, $\sigma_{zz}(x, z, t) \rightarrow -p$, where p is the local fluid pressure in

the fracture, whereas $\sigma_{zx}(x, 0, t) \rightarrow -\tau_{wall}$, the shear stress resisting the turbulent fluid flow in the fracture. Typically, in such hydraulic fracture situations, $\tau_{wall} \ll p$ and we follow [39] in neglecting τ_{wall} in comparison to p . Thus, recognizing $\Delta u_z(x, t)$ as $h(x, t)$, the opening gap along the fracture, the hydraulic fracture problem is formulated, like in [39], as

$$\left\{ \begin{array}{c} 0 \\ -p(x, t)/E' \end{array} \right\} = \int_{-L(t)}^{+L(t)} \left(\begin{array}{cc} K_{xx}(x-x', 0^+) & K_{xz}(x-x', 0^+) \\ K_{zx}(x-x', 0^+) & K_{zz}(x-x', 0^+) \end{array} \right) \frac{\partial}{\partial x'} \left\{ \begin{array}{c} \Delta u_x(x', t) \\ h(x', t) \end{array} \right\} dx' \quad (3.3)$$

which ultimately relates the pressure distribution $p(x, t)$ within the fracture to its opening gap $h(x, t)$ along it.

Consistent with the high Reynolds number estimated in Eq. 3.1, the flow in the fracture is expected to be a turbulent flow in a rough-walled gap. The relevant considerations are, first, that the Darcy-Weisbach friction factor f , for such flows at mean velocity U in rough-walled pipes or channels, is defined by writing the wall shear stress resisting the flow as $\tau_{wall}/(\rho U^2/2) = f/4$ (ρ is the density of the fluid, water in our case). That f may be estimated for the present case of flow in a thin slit by using well-calibrated data for flow in rough-walled cylindrical pipes, reinterpreted for a slit using the hydraulic radius concept. Following [40], that gives $f \approx 0.143(k/h)^{1/3}$ where k is the amplitude of the wall roughness as an equivalent Nikuradse grain size. An insightful recent discussion on such

turbulent flow in rough-walled tubes is given by Gioia and Chakraborty [18]; see also [36].

Observing that the gap h times the pressure gradient $-\partial p/\partial x$ is equilibrated by $2\tau_{wall}$, we have

$$-h \frac{\partial p}{\partial x} = 0.0357 \rho U^2 (k/h)^{1/3} \quad (3.4)$$

(here, ρ is the mass density of the water; we use ρ_{ice} below for the lesser mass density of the ice).

To the preceding Eq. 3.3 and Eq. 3.4 we add the conservation of mass,

$$\frac{\partial(hU)}{\partial x} + \frac{\partial h}{\partial t} = 0 \quad (3.5)$$

to close the system, as the set of equations in fluid pressure p , fracture opening gap h , and fluid velocity U that was formulated and solved numerically in [39] (and earlier for the $L \ll H$ range in [40]).

3.4 APPLICATION TO BASAL FRACTURE PROPAGATION

Here we present the solutions to the above system of equations, as devised in [39], and use them subsequently to address the time scale of glacial under-flooding in the lake drainage event considered.

The rate of fracture propagation along the bed is

$$\frac{dL}{dt} \equiv U_{tip} = \left(\frac{p_{inlet} - \sigma_o}{\rho} \right)^{1/2} \left(\frac{p_{inlet} - \sigma_o}{E'} \right)^{2/3} \left(\frac{L}{k} \right)^{1/6} \phi \left(\frac{L}{H} \right). \quad (3.6)$$

Here the notation is a reminder that the fracture growth rate is assumed equal to the fluid velocity at the tip, and the function $\phi(L/H)$, as fitted to the numerical results of [39], is

$$\phi(L/H) \approx 5.13[1 + 0.125(L/H) + 0.183(L/H)^2]. \quad (3.7)$$

The polynomial in L/H in the brackets closely fits results of [39] out to $L/H = 5$, that is to $L \approx 5\text{km}$. Here σ_o is given by

$$\sigma_o \equiv \rho_{ice}gH, \quad (3.8)$$

the overburden pressure of the ice (which p_{inlet} must evidently exceed in order for water to be driven beneath the ice sheet to open the fracture). Note that in the absence of vertical flow, $p_{inlet} = \rho gH$, and since the liquid water density $\rho \approx 1.1\rho_{ice}$, $p_{inlet} > \sigma_o$ under those hydrostatic conditions, which is what drives the water to the bed.

Further, for a given inlet pressure p_{inlet} , the average h_{avg} of the opening gap $h(x, t)$ along $-L(t) < x < +L(t)$, i.e., along the fracture, is expressible in terms of p_{inlet} and L , as

$$h_{avg} \approx 1.72 \frac{p_{inlet} - \sigma_o}{E'} L [1 + 0.517(L/H)^2]. \quad (3.9)$$

Here the expression in the brackets closely fits numerical results of [39] up to $L/H = 3.5$, but falls about 15 percent too low at $L/H = 5$.

To estimate the volumetric inflow rate Q_{basal} (units $[L^3]/[T]$) to the bed, we choose some representative width W perpendicular to the diagram of Fig. 3.3 (i.e., in the unmarked y direction) over which the inflow rate (units $[L^2]/[T]$) per unit distance perpendicular to the plane of the diagram, calculated from the 2D plane strain solution of [39], may be assumed to apply approximately. We take $W = 3\text{km}$ for that width, noting that the major crevasse marked in Fig. 3.1 extends over a length of 2.7 km along the lake bed, and anticipating that the flow extended the lift of the ice off from its bed somewhat beyond the end of that feature. (Ultimately, a 3D analysis is needed, but that is well beyond the scope of this paper.) Thus, noting that $2LWh_{avg}$ is the volume of water in the subglacial fracture,

$$\begin{aligned} Q_{basal} &= \frac{d(2LWh_{avg})}{dt} \\ &= 6.88 \frac{(p_{inlet} - \sigma_o)}{E'} WL \left(1 + 1.034 \frac{L^2}{H^2} \right) \frac{dL}{dt} \end{aligned} \quad (3.10)$$

where dL/dt is given by Eq. 3.6, with Eq. 3.7, above. We note that for a given L/H , $dL/dt \propto (p_{inlet} - \sigma_o)^{7/6}$, and thus

$$Q_{basal} \propto (p_{inlet} - \sigma_o)^{13/6}. \quad (3.11)$$

3.5 COUPLING TO LAKE WATER SUPPLY TO THE BED BY A VERTICAL CRACK-CREVASSES SYSTEM

By mass conservation, the volumetric flow rate Q_{basal} into the basal fracture must equal Q_{vert} (see Fig. 3.3), the volumetric flow rate at which lake water flows down the vertical crack-crevasse system (which forms a feeder channel to the basal fracture). We assume that this vertical system has a width in the y direction (perpendicular to the plane of the diagram in Fig.3.3) which is the same width W as adopted above for the basal fracture. Also, for simplicity in making elementary estimates of the lake drainage time scale, we model this vertical feeder channel as having a spatially uniform opening gap $\Delta\bar{u} = \Delta\bar{u}(t)$, thought of as the area-averaged opening of a vertical crack of depth $H \approx 1$ km in the z direction and width $W \approx 3$ km in the y direction, with faces loaded by the area-average pressures.

We determine the vertical flux using an elementary balance of forces on a vertical slab of water from the lake, of area HW and thickness $\Delta\bar{u}$, moving downward with velocity $U_{vert} (= Q_{vert}/W\Delta\bar{u})$. The flow is driven downward by the slab weight $\rho g HW \Delta\bar{u}$, which is balanced by the sum of the upward force $p_{inlet} W \Delta\bar{u}$ at the base of the slab and the shear forces from the wall shear stresses on the two vertical boundaries summing to $2\tau_{wall} HW$ where $\tau_{wall} = \rho(f/8)U_{vert}^2$ and $f = 0.143(k/\Delta\bar{u})^{1/3}$. Balancing

these forces leads to,

$$\rho g H W \Delta \bar{u} = (f/4) \rho U_{vert}^2 H W + p_{inlet} W \Delta \bar{u}, \quad (3.12)$$

which can be rearranged to give the formula for the vertical flux

$$Q_{vert} \approx 5.29 \left(1 - \frac{p_{inlet}}{\rho g H} \right)^{1/2} W \Delta \bar{u}^{3/2} g^{1/2} \left(\frac{\Delta \bar{u}}{k} \right)^{1/6}. \quad (3.13)$$

In a somewhat similar attempt to link flow down the vertical crevasse to flow into the basal fracture, Tsai and Rice [40] assumed, in view of the relatively short time scale (< 1.5 hr) of rapid drainage, purely elastic response of the vertical crevasse, with its opening being proportional to the difference between the average pressure $p_{inlet}/2$ in the crevasse and the corresponding average $\sigma_o/2$ for the far-field horizontal stress in the ice. That led to the unphysical result of eventual complete crevasse closure when assuming purely elastic response of the ice (which is discussed below).

To more accurately model the drainage, particularly regarding the previous assumption of purely elastic ice deformation, we allow here for the possibility of significant creep opening of the crevasse. To motivate this, recall that slow falling of the lake level was observed for ≈ 16 hrs before the rapid break-out. We interpret that fact here as evidence that the crevasse system may have been highly pressurized before nucleation of the propagating basal fracture at the bed. Thus, we quantify this creep

opening of the crevasse before nucleation of the basal fracture. (That nucleation process would, of course, be sensitive to the value of K_{lc} , or some generalization of it for the ice-rock interface, but we are not able to address it here.) Specifically, we write the crevasse opening $\Delta\bar{u}$ as having an elastic part plus a creep part,

$$\Delta\bar{u} = \Delta\bar{u}^{el} + \Delta\bar{u}^{cr}. \quad (3.14)$$

The creep part $\Delta\bar{u}^{cr}$ will depend on how long the crevasse faces have been pressurized prior to basal fracture nucleation, and is assumed to not change significantly during the short time scale of the lake drainage.

The elastic average opening can be derived from a 2D plane strain elastic solution for a crack of length W , opened by uniform pressure taken as $p_{inlet}/2$, in a medium under far-field compressive stress $\sigma_o/2$

$$\Delta\bar{u}^{el} = \frac{\pi(p_{inlet} - \sigma_o)}{4E'}W. \quad (3.15)$$

We define C as the ratio of the prior creep opening $\Delta\bar{u}^{cr}$ over the 16 hours of slow drainage to the elastic opening $\Delta\bar{u}^{el}$. In that comparison both are evaluated for hydrostatic pressure $p_{inlet} = \rho gH$ (see Eq. 3.17 to follow). Inserting this formula for the average conduit opening into our formula for the vertical flux given in Eq. 3.13, we can write Q_{vert} as a function of p_{inlet} alone. This is shown in Fig. 3.4 for the parameters given in Tab. 3.1. We see that the vertical flux increases with C

and has a non-monotonic dependence on the inlet pressure. Furthermore, Q_{vert} vanishes when the inlet pressure is equal to ρgH . This figure nicely highlights the competing physical processes that control the flux through the vertical conduit. On the one hand, raising the inlet pressure increases elastic opening of the conduit promoting additional flow. However, raising the inlet pressure also lowers the pressure gradient driving flow, thus suppressing flow. Balancing these two considerations leads to peak fluxes that occur for an intermediate inlet pressure lying between $\sigma_o (= \rho_{ice}gH)$ and ρgH . Note that for $C = 0$ – corresponding to a conduit that undergoes only elastic opening – we also see low fluxes for inlet pressures near $\sigma_o = \rho_{ice}gH$ because the conduit closure chokes the flow.

To estimate the prior creep opening, we represent the creep deformation of the ice sheet by the Glen law form typically adopted in glaciology [8]. This is $d\gamma/dt = 2A_{cr}(T)\tau^n$, with $n = 3$, where τ is the Mises equivalent shear stress, based on the second invariant of the deviatoric stress tensor $s_{\alpha\beta}$, and $d\gamma/dt$ is the equivalent engineering shear strain rate, with the trace of the creep strain rate vanishing (no volumetric creep strain) and with components of deviatoric strain rate being in proportion to one another just as are components of $s_{\alpha\beta}$. Recommended values of $A_{cr}(T)$ are given by Cuffey and Paterson [8], and within the simplicity of our modeling, we evaluate $A_{cr}(T)$ based on a single value of T , hoped to be representative of ice temperatures in the vicinity of the lake and

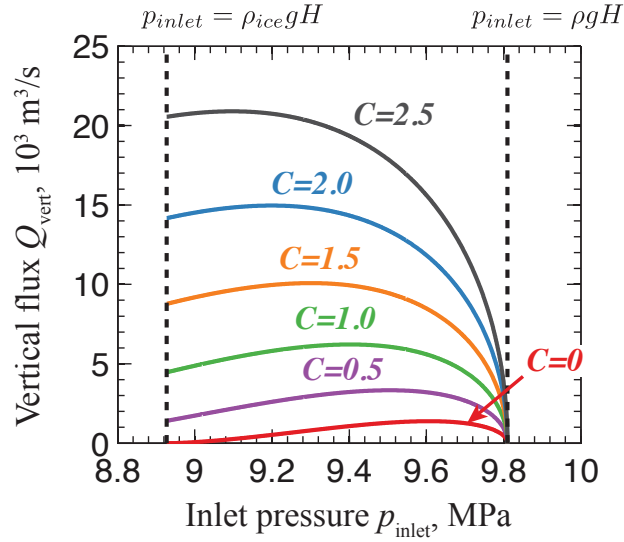


Figure 3.4: Dependence of flow rate on inlet pressure for several values of the creep parameter C . In the model, the flow begins at $p_{inlet} = \rho g H$ (hydrostatic pressure), but then the pressure drops as flow rate develops, until the pressure p_{inlet} falls to the ice overburden pressure $\rho_{ice} g H$.

crevasse system. We note that $A_{cr}(T)$ remains finite for the solid phase of ice at its melting temperature.

Although there is no general analytical solution for crack opening in a material undergoing power law creep (except in the linear viscous case), we use the following approach. Based on solutions for pressurized circular holes, elliptical holes, and flat cracks in the $n = 1$ linear viscous case (analogous to familiar linear elastic solutions, but evaluated with $\nu = 1/2$), and the Nye [29] solution for a pressurized circular hole in a power law creeping material, Fernandes and Rice (in progress) have conjectured that the average creep opening rate of a pressurized crack

of length W in plane strain, opened by uniform pressure taken as $p_{inlet}/2$, in a power-law creeping solid under far-field compressive stress $\sigma_o/2$, could be represented as

$$\frac{d\Delta\bar{u}^{cr}}{dt} = \kappa(n) \frac{\pi}{2} A_{cr}(T) \left(\frac{p_{inlet} - \sigma_o}{2n} \right)^n W \quad (3.16)$$

where $\kappa(n)$ is a correction factor depending on n , which is expected to be close to 1.0 (and is 1.0 in the $n = 1$ case).

In numerical simulations we compared results from the above approximation to a plane-strain finite element model of a pressurized crack using *ABAQUS*. That was formulated as a Maxwell model (elastic and viscous elements in series, where the viscous elements satisfy power law creep), so that when solved within small geometry change assumptions, the displacement rates converge in time to those of a purely viscous material. This approach allows the model to respond to suddenly applied and sustained boundary loading but on a time scale before the crack has opened enough to respond differently from a straight cut. In order to isolate the creep strain rate using the *ABAQUS* elastic plus creep deformation formulation, we waited long enough for essentially steady state creep strain rate to be achieved and elastic relaxation to be completed. See [6, 28] for other computational approaches to creep flow. The simulation was benchmarked using two simple tests: (1) Comparing the opening rate of the crack under linear viscous deformation ($n = 1$) to the known analytical solution. Results yield an average nominal nodal

error of 0.03 % with a maximum nodal error of 0.1% nearest the crack tip. (2) Using a model assuming a nonlinear rheology ($n = 3$) generate results which were found to compare favorably to the HRR field described by Hutchinson [22] and Rice and Rosengren [33]. By comparing the approximation in Eq. 3.16 to the numerical solution attained from the *ABAQUS* model, the correction factor $\kappa(n)$ was found, for the $n = 3$ case of interest in this study, to be $\kappa(3) \approx 0.8$.

We estimate $\Delta \bar{u}^{cr}$ at the time of basal fracture nucleation, after approximately 16 hours of slow leakage from the lake, by assuming hydrostatic pressurization of the vertical crevasse system ($p_{inlet} = \rho g H$) for that 16 hour period, hence multiplying $d\Delta \bar{u}^{cr}/dt$ above by 16 hours. As noted, a scale for the resulting $\Delta \bar{u}^{cr}$ is to compare it to the $\Delta \bar{u}^{el}$ corresponding to hydrostatic pressurization of the vertical crevasse, giving C as

$$C = \left(\Delta \bar{u}^{cr} \Big|_{p_{inlet}=\rho g H}^{t=16\text{hr}} \right) / \left(\Delta \bar{u}^{el} \Big|_{p_{inlet}=\rho g H} \right) . \quad (3.17)$$

Note that C scales linearly with time t of hydrostatic pressure, with $A_{cr}(T)$, and with H^2 (when $n = 3$). Also, $A_{cr}(T)$ has a weak dependence on ice pressure P [8] which we choose as $P = \sigma_o/2$. Assuming $H = 1$ km, $E' \approx 6.8$ GPa, $n = 3$, and $\kappa(3) = 0.8$, we consider (being mindful that, as we show in the next section, the best-fitting C to match the discharge data are in the range of $C = 1.5$ to 2.0) average ice temperatures in the range -7.0°C to -5.0°C . The corresponding A_{cr} are $A_{cr}(-7^\circ\text{C}) = 6.32 \times 10^{-25} \text{s}^{-1} \text{Pa}^{-3}$ and $A_{cr}(-5^\circ\text{C}) = 9.31 \times 10^{-25} \text{s}^{-1} \text{Pa}^{-3}$. With those

parameters, and with $H = 1$ km, and standard values of ρ and ρ_{ice} , we obtain $C = 1.42$ at -7.0°C , and $C = 2.11$ at -5.0°C , which closely bracket that preferred range of C . Similarly, we obtain temperatures corresponding to relevant C values of $C = 1.50$ as $T = -6.75^\circ\text{C}$ and $C = 2.00$ as $T = -5.27^\circ\text{C}$ (see Tab. 3.1).

In the calculations of the next section, we recognize that the creep opening does not change appreciably during the short time scale of lake drainage, and therefore represent the total crevasse opening $\Delta\bar{u}$ (as needed in Eq. 3.12 above to characterize resistance to flow down the crevasse) as

$$\Delta\bar{u} = \frac{\pi(p_{inlet} - \sigma_o)}{4E'}W + C\frac{\pi(\rho gH - \sigma_o)}{4E'}W \quad (3.18)$$

where $\sigma_o = \rho_{ice}gH$. A recent study addresses in another context how a pre-existing subglacial drainage system interacts with fluid penetration along it [2].

3.6 ESTIMATING THE TIME SCALE FOR LAKE DRAINAGE

In this section we estimate the time scale for lake drainage using our model for combined flow in the vertical conduit and basal fracture. Eq. 3.6 is solved for the evolution of the basal fracture using an inlet pressure p_{inlet} found by coupling the vertical conduit with the basal fracture through

$$Q_{basal} = Q_{vert}. \quad (3.19)$$

Using Eq. 3.10 and Eq. 3.13 this can be rearranged to find an equation for the inlet pressure

$$0.15 \left(\frac{\pi W}{4H} \right)^{5/3} ((\rho - \rho_{ice})gH - \Delta p)^{1/2} (\Delta p + C(\rho - \rho_{ice})gH)^{5/3} = \Delta p^{13/6} F(L/H), \quad (3.20)$$

where we have defined the excess inlet pressure to be $\Delta p = p_{inlet} - \rho_{ice}gH$ and the function

$$F(x) = x^{7/6} (1 + 0.125x + 1.218x^2 + 0.129x^3 + 0.189x^4). \quad (3.21)$$

For $C = 0$, Eq. 3.20 can be solved analytically, allowing p_{inlet} to be written as a function of L . This turns Eq. 3.6 into a single ordinary differential equation for the length of the basal fracture L that is solved using built-in MATLAB routines. The solution is slightly more complicated when $C \neq 0$ and Eq. 3.6 and Eq. 3.20 must be solved simultaneously. It can be shown that Eq. 3.6 and Eq. 3.20 form a system of differential-algebraic equations of index 1, leading to two possible solution methods. The first method involves treating Eq. 3.6 as a single ODE while solving the algebraic equation at each time-step using standard root finding methods, and the second method involves differentiating Eq. 3.20 with respect to time to yield an ODE for p_{inlet} that is solved alongside Eq. 3.6. Both methods were tested and found to give consistent results, though all results shown from this point onwards were produced using the root

finding method.

Fig. 3.5 shows the evolution of L and p_{inlet} for the parameters given in Tab. 3.1 and a range of values of C between zero and two. As shown later, for the largest values of C the lake can completely drain. When total drainage occurs we terminate the solutions and indicate this by a solid circle in Fig. 3.5. We observe that the basal fracture grows to a length of several kilometers within a few hours, with larger values of C leading to faster fracture growth. This is to be expected since a larger value of C corresponds to a wider vertical conduit, and thus a larger water flux delivered to the basal fracture. Interestingly, we observe that the inlet pressure is relatively insensitive to changes in C , with the inlet pressure typically close to the ice overburden σ_o . However, the sensitive dependence of U_{tip} on the difference between p_{inlet} and σ_o turns this small difference in excess pressure into a pronounced difference in basal fracture length. The small excess pressures shown in Fig. 3.5 means that elastic opening of the vertical conduit is typically small when compared to the opening due to creep in the period immediately before rapid drainage commences. This is shown in Fig. 3.5 where we observe that the average conduit opening quickly returns to $\Delta\bar{u} = \Delta\bar{u}^{cr}$ as the inlet pressure falls towards σ_o . We do not show the evolution of conduit opening for $C = 0.5$ and $C = 1.5$ since it is qualitatively similar to the solutions for $C = 0, 1$ and 2 , with the average conduit opening falling to $\Delta\bar{u}^{cr}$ over a time scale of approximately half an hour.

Parameter	H	W	ρ	ρ_{ice}	g	k	E'	n	t	$A_{cr}(-7^\circ\text{C})$	$A_{cr}(-5^\circ\text{C})$
Value	1	3	1000	910	9.81	0.01	6.8	3	16	6.32×10^{-25}	9.31×10^{-25}
Unit	km	km	kg/m ³	kg/m ³	m/s ²	m	GPa	-	hrs	Pa ⁻³ s ⁻¹	Pa ⁻³ s ⁻¹

Table 3.1: A table summarizing the parameter values used in this manuscript. All parameters choices follow those made in [40] except for the creep parameters which follow [8].

Using our solution for L and p_{inlet} we can calculate the water flux from the lake and into the basal fracture using Eq. 3.13. The evolution of this flux is also shown in Fig. 3.5. We observe that at the onset of rapid drainage the flux increases rapidly before reaching a state where the flux remains almost constant. Our results show a strong dependence of the water flux on C , which is to be expected when elastic opening of the vertical conduit is small. Importantly, in the solution for $C = 0$, where creep is neglected and all opening of the conduit is elastic, we see that the conduit quickly closes as the inlet pressure drops preventing the lake from draining. In Fig. 3.5 we indicate the average water flux of $\sim 8700 \text{ m}^3/\text{s}$ inferred in [10] using a dashed line and find that this is best matched by the solution with $C = 1.5$.

Our calculations for the water flux into the basal fracture can be used to predict how the lake surface height drops once rapid drainage begins. To do this we must first make some assumptions about the geometry of the lake. We assume an axisymmetric lake with a parabolic shape, which allows us to relate the radius of the lake r at a given distance below the lake surface z , where z is taken to be positive in the upwards direction

and zero at the initial lake surface. For this parabolic shape,

$$r^2 = \hat{\alpha}(z + D) \quad , \quad \hat{\alpha} = \frac{A_{init}}{\pi D}, \quad (3.22)$$

where D is the initial lake depth and $\hat{\alpha}$ is a constant determined using observations of the initial lake surface area A_{init} . This allows us to find the area of the lake at any depth z and initial lake volume

$$A(z) = \frac{A_{init}(z + D)}{D} \quad , \quad V_{init} = \frac{DA_{init}}{2}. \quad (3.23)$$

Thus using the measurements of $A_{init} = 5.6 \text{ km}^2$ and $V_{init} = 44 \times 10^6 \text{ m}^3$ from [10] we estimate the initial lake depth to be $\sim 15.7 \text{ m}$.

Having approximated the lake geometry and estimated the initial depth we now model the lake drainage using our solution for Q_{vert} and rewrite this in terms of the lake surface height using our solution for $A(z)$ to find

$$\frac{dV}{dt} = -Q_{vert}(t) \quad , \quad \frac{dz}{dt} = -\frac{DQ_{vert}(t)}{A_{init}(z + D)}. \quad (3.24)$$

where V is the current volume of water in the lake. To conclude we try to match our model with the observations of a falling lake surface from [10]. Fig. 3.6 shows how the lake depth drops for the parameters given in Tab. 3.1 and $C = 2$. To find this optimal value of C we tested a range of values with a spacing of 0.1 We find reasonable agreement with the observational data for the period of most rapid drainage but are unable

to match the gradual onset of drainage shown in the data.

3.7 CONCLUSIONS

We have reviewed understanding of the coupled fluid and solid mechanics underlying an important class of natural hydraulic fractures, involving rapid lake drainages through and under ice sheets and glaciers by turbulently flowing meltwater.

Our particular focus was on the 2006 rapid drainage event at a well-instrumented supraglacial lake, of $\sim 44 \times 10^6 \text{ m}^3$ volume, on the Greenland Ice Sheet. Once rapid drainage began, the lake drained into the ice within 1.0 to 1.5 hours.

We showed that our modeling of the drainage time has good correspondence with observational constraints on the rapidity of drainage. Although it is reasonable to assume that the ice responds elastically on such a short time scale, we noted that there was ~ 16 hours of slow drainage (shown by $\sim 15 \text{ mm/hr}$ fall in lake level), before the breakout to rapid drainage.

Therefore, using standard temperature dependent power-law creep modeling of ice, we quantified possible slow creep opening over that 16 hr period, due to hydrostatic pressurization of a vertical crack-like crevasse system, 2.7 km long as exposed at the surface, which connects the lake bottom to the glacial bed, 1 km below. The crevasse is presumed

to be the main conduit for the water.

A creep parameter C was introduced, giving the ratio of the creep opening to what would be the elastic opening of that same vertical crack-crevasse if its surfaces were loaded by hydrostatic fluid pressure. Values of C in the range 1.5 to 2.0 were shown to give an excellent fit to the observations; the former best predicts the average flux of water out of the lake (Fig. 3.5, lower right), whereas the latter best fits the maximum observed rate of lake level descent (Fig. 3.6).

Using data on the temperature dependence of creep, we concluded that ice in the vicinity of the lake would have to respond as if it had a temperature in the range -7.0 to -5.0°C to produce such values of C .

GPS measurements were also reported in Figure 2C of [10] and it is not yet clear that our present style of modeling, even if improved in sophistication, can fully explain them. They show that the ice sheet was moving primarily to the west with a slight northern trend (at 6% of the westward motion) prior to the rapid drainage event. The event itself caused a rapid 0.8 m displacement of the GPS site to the north, which was followed by its gradual return south over the next two days, after which the primarily westward pre-event motion was recovered.

Based on that pre-event motion, we must assume that the shear traction on the base of the ice sheet was primarily eastward-directed prior to the hydraulic fracture and lake drainage. Further, if the vertical crack/crevasse system (Fig. 3.1) became highly pressurized over a multi-hour period

before the basal hydraulic fracturing, the deformation caused by that pressurization was resisted not just by the stress-dependent creep flow within the ice sheet (which we have modeled here), but also by the development of a component of traction at the base of the ice sheet. That would be a traction component in a direction approximately orthogonal to the pre-event eastward traction, and its development is expected to attenuate the short term creep motion of the ice sheet in a manner consistent with the minimal observed northward displacements at the GPS site prior to the hydraulic fracture. At present, we have no good procedure to describe that process and its effect on the creep opening, which we have modeled here as if there was no basal shear resistance.

However, an assumption of no (or negligible) basal shear resistance is reasonable over the part of the base that is being hydraulically fractured, and hence for assessing the elastic part of the response to crack/crevasse opening. It is clear that a fuller analysis of the basal creep mechanics and shear resistance, in a manner which also rationalizes the GPS observations, is a significant goal for future clarification.

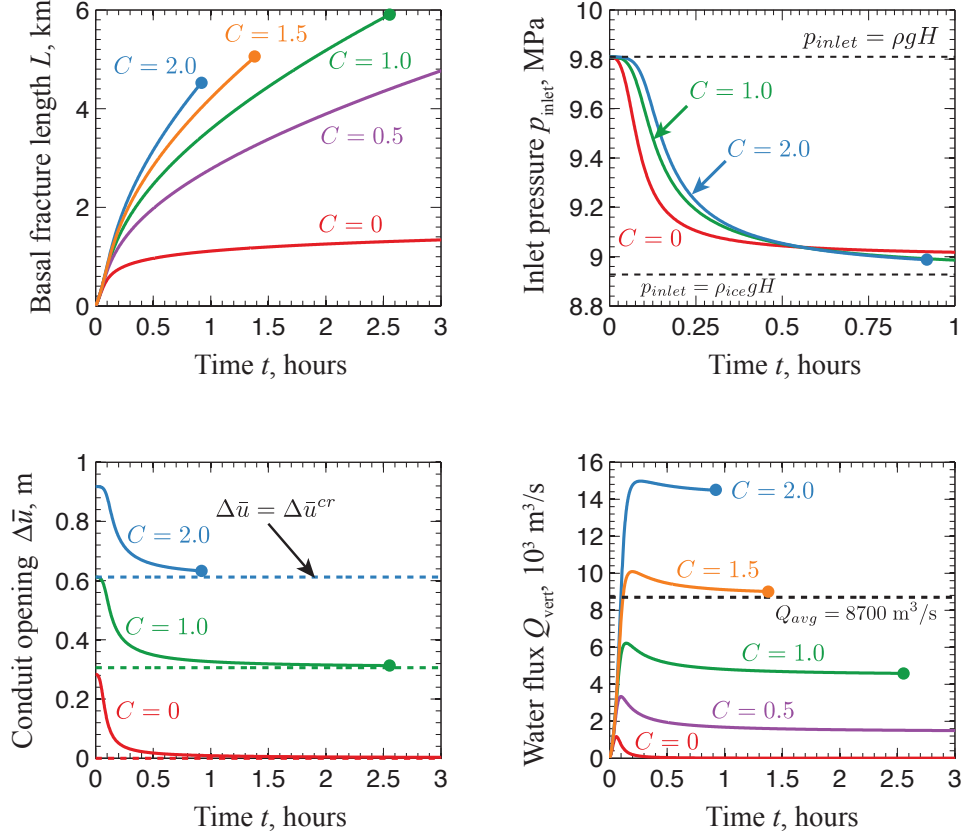


Figure 3.5: A plot showing how the basal fracture length, inlet pressure, conduit opening, and water flux into the basal fracture evolve for a range of values of C between 0 and 2.0. Dots at the ends of the curves mark complete drainage of the lake. These results were produced using the parameters given in Tab. 3.1. We see that the flux into the fracture increases with C , leading to more rapid growth of the basal fracture. The average flux of $8700 \text{ m}^3/\text{s}$ inferred in [10] is plotted as a dashed line. Our results also show that inlet pressures quickly fall from the initial hydrostatic value to close to σ_o and this is accompanied by elastic closing of the conduit opening.

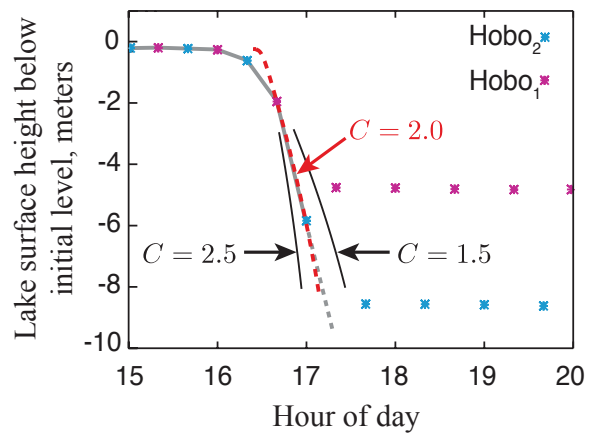


Figure 3.6: Data from the 2006 lake drainage event reproduced from Das et al. [10] with an additional curve showing our model prediction for the parameters given in Tab. 3.1 and $C = 2.0$, meaning that the creep opening is twice what would be the initial elastic opening of the crack-crevasse system if subjected to hydrostatic water pressure.

This project was a collaboration with Colin R. Meyer and Professor James R. Rice. My role in this project was to construct all of the numerical simulations involving the coupled in-plane and antiplane solutions. My role was also to benchmark the analytical solutions and assure that the numerical solutions matched the expressions derived in the paper. The work in this chapter has been submitted for publishing at the Journal of Fluid Mechanics and is currently under review.

Meyer, C.R., Fernandes, M.C., and Rice, J.R.(2015, *Submitted*). R  thlisberger channels under antiplane shear. *Journal of Fluid Mechanics*.

4

R  thlisberger channels under antiplane shear

4.1 ABSTRACT

We examine superimposed antiplane shear on the in-plane creep closure of a R  thlisberger channel, a meltwater conduit that is maintained

due to a balance between turbulent heat dissipation melting the channel walls and in-plane viscous creep closure of the ice. Although the shearing does not factor explicitly in the in-plane creep closure, it enters through the effective viscosity when assuming that ice deforms as a power-law shear-thinning fluid with a rheological power given by Glen's law. We first develop a closed-form small perturbation solution, for which the amount of superimposed antiplane shear strain rate is much smaller than the in-plane strain rate. At linear order, the antiplane shear perturbation has no effect on the creep closure of the Röthlisberger channel because the effective viscosity is set by the in-plane creep closure. The far-field is examined in two ways. We first consider a finite domain where the outer radius must satisfy an inequality for the perturbation solution to be valid. Then, we consider an infinite domain and find that even for small amounts of antiplane shear there exists an in-plane dominated region and an antiplane dominated region. These solutions are verified numerically. We also examine the limit where the antiplane strain rates dominate the in-plane strain rates, and find a simple scaling for the average creep closure velocity. We numerically compute the strain rate concentration factors from the in-plane dominant range up to the fully antiplane regime. Then, using numerics, we compute the viscous creep closure and determine the size of the Röthlisberger channel as a function of the superimposed antiplane shear.

4.2 INTRODUCTION

Liquid water is fundamental to glaciers and ice sheets because it facilitates sliding at the glacier base. The connection between ice motion and subglacial hydrology motivates us to examine the influence of shear in the ice on the size of meltwater channels. These channels, called Röthlisberger channels, are formed by turbulently flowing liquid water and are easily visible, stunning features of the cryospheric landscape. Röthlisberger channels are of great interest in subglacial hydrology for their ability to transport large volumes of water [7, 16]. The mathematical theory describing their formation dates back to a series of papers presented at a symposium on the hydrology of glaciers held at Cambridge University in 1969. Röthlisberger [35] outlines the theory and other significant contributions are presented in Shreve [37] and Weertman [45]; a full account of the history is given in Walder [44]. In Röthlisberger channel theory, liquid water, which is at the melting temperature, flows turbulently through a circular (or half-circular) conduit. The turbulent eddies dissipate heat at the wall and melt the ice, increasing the size of the channel. Simultaneously, the mass of ice surrounding the channel viscously creeps inward, closing the hole. In equilibrium the creep closure of the ice is exactly balanced by the melting incurred by the turbulence.

Nye [29] derives the creep closure velocity u_r of the ice for a circular conduit in polar coordinates, which is

$$u_r(r) = -A \left(\frac{\Delta p}{n} \right)^n \frac{a^2}{r}, \quad (4.1)$$

where a is the radius of the channel and Δp is the hydrostatic ice overburden pressure less the water pressure. The factors A and n come from the assumed rheology: ice can be modelled as a shear-thinning fluid with a power-law relationship between deviatoric stress and strain rate, $\dot{\epsilon}_E = A\tau_E^n$, with ice softness A and the rheological power n (where $n = 3$ is Glen’s law), and the subscript E indicates the second invariant of the tensor (discussed more in the next section). Nye [29] compared the predictions from equation (4.1) to published data on the closure of tunnels in a variety of glaciers. Nye found that the closure expression fit most glaciers quite well with the exception of the Mont Collon icefall on the Arolla Glacier—presumably due to superimposed stresses induced by the icefall. Glen [19] also considered the deformation of a tunnel near an icefall: as part of the 1955 Cambridge Austerdalsbrae Expedition to study ogives, a tunnel was drilled into the icefall and creep closure measured. Glen [19] found that there is a considerable compressive stress within the ice and the creep closure rates are even larger than the Arolla Glacier data from Nye [29] as well as further from the Nye solution in equation (4.1). Motivated by these field observations, Weertman [45] considered meltwater conduits theoretically. Building on the analysis

by Nye [29], Weertman noted that the closure of a fully circular channel (ice surrounds water) is identical to the closure of a half-circular channel (the common model for a Röthlisberger channel: half-circle cut out of ice and bounded by bedrock/till on the bottom) so long as there is no in-plane shear stress along the base of the glacier. Only fully circular channels are considered in this paper.

Röthlisberger channels in subglacial hydrology systems are crucial to ice movement in Greenland and Antarctica. Surface velocity data show that ice drainage in Antarctica is not uniform but rather punctuated by regions of fast flowing ice called ice streams [24]. At the margins of these ice streams, the ice is strongly sheared which softens the ice due to its shear-thinning rheology (with more shear stress, resistance to flow decreases.) Simultaneously, shearing temperate ice, i.e. ice at the local melting temperature that maintains some mechanical strength, produces meltwater through viscous heating, which is efficiently evacuated through a Röthlisberger channel. There is observational evidence for moving water beneath an ice stream shear margin [43]. Theoretically, Perol and Rice [30] describe how channels can interact with the subglacial hydrologic system to partially stabilise the shear margin against lateral expansion. With this in mind, we examine the effect of antiplane shear induced by the ice stream on the creep closure of a Röthlisberger channel at an ice stream shear margin. We show that the amount of antiplane shear present in the ice can substantially increase the size of

Röthlisberger channels.

This paper is organised in the following way: First we describe Glen's law, an appropriate rheology for ice under conditions typically encountered in glaciology (section 4.3). Then, we describe the equations and boundary conditions for superimposed antiplane shear on in-plane motion for a finite domain. We nondimensionalise these equations and identify a strain rate ratio S that indicates the importance of antiplane shear to in-plane strain rate. For small strain rate ratios, we derive the finite domain Nye solution. Then, since the strain rate ratio is small, the viscosity is dominated by the Nye solution and we can solve for the antiplane velocity (section 4.4.1). For this perturbation solution to be valid in the finite domain, we find an inequality that relates the domain size, the strain rate ratio and the rheology. Numerically, we then compute the strain rate concentration factor as a function of the strain rate ratio (section 4.4.2). We then turn to the infinite domain and examine the transition between in-plane dominated and antiplane dominated domains (section 4.4.3). Then we move to the large strain rate ratio limit and consider perturbation channel creep closure velocities and find a simple scaling for the creep closure velocity and the strain rate ratio (section 4.4.4). Finally, we bring together all of these results to show how the Röthlisberger channel size depends on the strain rate ratio (section 4.5).

4.3 ANALYSIS

Here we describe the equations for the combined in-plane and antiplane motion around a hole under plane strain conditions and then nondimensionalise them. The boundary conditions for a finite domain, in dimensional and nondimensional form, are depicted in figure 4.1. We start by examining the rheology of ice. Treating ice as a homogeneous, incompressible simple fluid, we can use a power-law relationship between effective stress and effective strain rate, given by

$$\dot{\epsilon}_E = A\tau_E^n, \quad (4.2)$$

where $\dot{\epsilon}_E$ is effective strain rate (second invariant of the strain rate tensor), A is the ice softness (spatio-temporally independent for a constant temperature), τ_E is the effective stress (second invariant of the deviatoric stress tensor), and n is the rheological exponent ($n > 1$ for shear-thinning). The standard value used in glaciology is $n = 3$, which is called Glen's law. However, depending on the creep mechanism and the stress magnitude, values from $n = 1$ to $n = 4$ are more appropriate [12, 20]. Here we will primarily use arbitrary n for analysis and $n = 3$ for figures and discussions.

For combined plane and antiplane strain rates, the effective stress and

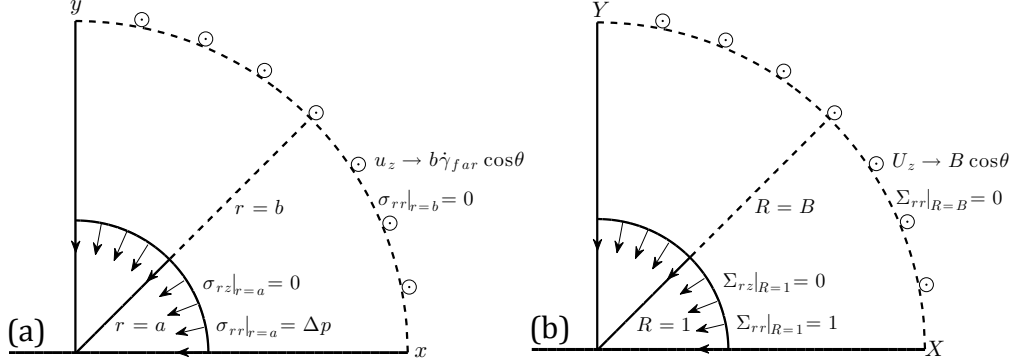


Figure 4.1: Physical space and boundary conditions for in-plane and antiplane motion around a channel: (a) dimensional and (b) nondimensional.

strain rate are given in polar coordinates as

$$\tau_E = \sqrt{\frac{1}{4}(\sigma_{rr} - \sigma_{\theta\theta})^2 + \sigma_{r\theta}^2 + \sigma_{rz}^2 + \sigma_{\theta z}^2} \quad \text{and} \quad \dot{\epsilon}_E = \sqrt{\dot{\epsilon}_{rr}^2 + \dot{\epsilon}_{r\theta}^2 + \dot{\epsilon}_{rz}^2 + \dot{\epsilon}_{\theta z}^2}. \quad (4.3)$$

Assuming co-axiality of the deviatoric stress and strain rate tensors, equation (4.2) then implies that

$$\dot{\epsilon}_{ij} = A \tau_E^{n-1} \left(\sigma_{ij} - \frac{1}{3} \sigma_{kk} \delta_{ij} \right), \quad (4.4)$$

where $\dot{\epsilon}_{ij}$ is the symmetric part of the velocity gradient tensor.

We first consider a finite domain from $r = a$ to $r = b$ as shown in figure 4.1. On the outer edge of this boundary, the normal stress is equal to the overburden (hydrostatic) pressure of the ice, $\sigma = -\rho_{ice} g H (1 - y/H)$, where H is the glacier thickness. Assuming that $y/H \ll 1$ and, therefore, that the overburden is constant around the hole, we write the constant

overburden pressure as $\sigma_o = -\rho_{ice}gH$. On the boundary of the channel, the normal stress is the water pressure inside the channel, $-p_w(> -\sigma_o)$. Due to incompressibility and the pressure independence of the assumed rheology, we can add to our stress field the uniform tensile stress $\sigma_{ij} = \sigma_o\delta_{ij}$, which has no effect on the flow field and removes any traction on the outer wall. This gives $\sigma_{rr}(r = a) = \sigma_o - p_w = \Delta p$ at the channel wall. Thus, the in-plane boundary conditions are

$$\sigma_{rr}(r = a) = \sigma_o - p_w = \Delta p, \quad \sigma_{rr}(r = b) = 0.$$

In the antiplane direction, i.e. into and out of the page, the shear stress on the inner channel is zero. On the outer boundary, we consider a linear strain rate that varies in strength with distance to represent far-field shearing. In this way, we write the antiplane boundary conditions as

$$\sigma_{rz}(r = a) = 0, \quad u_z(r = b) = \dot{\gamma}_{far}b \cos(\theta).$$

We can now nondimensionalise using capitalised characters to denote nondimensional quantities. Scaling all lengths by the channel radius a , we have $r = aR$ and the dimensionless outer radius $B = b/a$, which is the domain size. We can scale the antiplane shear strain rate by $\dot{\gamma}_{far}$ and the in-plane components of strain rate by $A\Delta p^n$, i.e. $\dot{\epsilon}_{rr} = A\Delta p^n \dot{E}_{rr}$. This strain rate scaling can be seen from the derivative of the Nye solution, equation (4.1). A consequence of this scaling is that the strain rates will

not necessarily be order one numbers. In the case of the Nye solution, at the edge of the channel $\dot{E}_{rr} = n^{-n}$, which is $1/27$ for $n = 3$ and is not order one. We can nondimensionalise the effective strain rate in the same way as the in-plane strain rates, which gives

$$\dot{E}_E = \sqrt{\dot{E}_{rr}^2 + \dot{E}_{r\theta}^2 + S^2 (\dot{E}_{rz}^2 + \dot{E}_{\theta z}^2)}, \quad (4.5)$$

where S is the strain rate ratio given as

$$S = \frac{\dot{\gamma}_{far}}{A \Delta p^n} \left(\frac{\text{antiplane}}{\text{in-plane}} \right) \quad (4.6)$$

This ratio represents the importance of the superimposed antiplane shear strain rate as compared to a characteristic in-plane strain rate. In the purely in-plane case, where no antiplane motion is superimposed, i.e. $S \ll 1$, the hoop strain rate at the edge of the channel is

$$\dot{\epsilon}_{\theta\theta}^{Nye} = A \left(\frac{\Delta p}{n} \right)^n.$$

Using this definition we can see that S is the ratio of strain rates:

$$S = \frac{\dot{\gamma}_{far}}{n^n \dot{\epsilon}_{\theta\theta}^{Nye}}. \quad (4.7)$$

We can also write S as a ratio of stresses. At the outer edge of the domain,

we define the antiplane shear stress τ_{far} as

$$\tau_{far} = \left(\frac{\dot{\gamma}_{far}}{2A} \right)^{1/n},$$

although τ_{far} only corresponds to the true antiplane shear stress at the edge of the domain when the ice is deformed in pure antiplane shear.

We can write S in terms of τ_{far} as

$$S = 2 \left(\frac{\tau_{far}}{\Delta p} \right)^n. \quad (4.8)$$

All three of these definitions for S , the primary definition (equation (4.6)), the strain rate interpretation (equation (4.7)), and stress ratio (equation (4.8)), are identical and show that $S = \dot{\gamma}_{far}/A\Delta p^n$ represents the importance of the antiplane strain rate imposed on the outer edge of the domain to the in-plane creep closure of the channel.

To nondimensionalise the stress components, we scale in-plane stresses by Δp so that $\sigma_{rr} = \Delta p \Sigma_{rr}$, antiplane stresses by $S\Delta p$ so that $\sigma_{rz} = \Delta p S \Sigma_{rz}$, and write the effective stress as $\tau_E = \Delta p T_E$, where

$$T_E = \sqrt{\frac{1}{4} (\Sigma_{rr} - \Sigma_{\theta\theta})^2 + \Sigma_{r\theta}^2 + S^2 (\Sigma_{rz}^2 + \Sigma_{\theta z}^2)}, \quad (4.9)$$

The velocities scale as the strain rates multiplied by the channel radius so that

$$u_r = Aa\Delta p^n U_r \quad \text{and} \quad u_z = Aa\Delta p^n S U_z. \quad (4.10)$$

The boundary conditions, in nondimensional form, are then

$$\Sigma_{rr}(R = 1) = 1, \quad \Sigma_{rr}(R = B) = 0, \quad \Sigma_{rz}(R = 1) = 0, \quad U_z(R = B) = B \cos(\theta).$$

4.3.1 REASONABLE STRAIN RATE RATIO VALUES

For mountain glaciers, we can estimate the size of the strain rate ratio S as

$$S \sim \frac{u_s}{AH\Delta p^n},$$

where u_s is the surface velocity and H is the glacier thickness. This scaling is an estimate of the shear induced by sliding with zero basal slip. If basal sliding is present then the difference in surface velocity u_s and basal sliding velocity u_b , i.e. $u_s - u_b$, would be a more appropriate velocity scale in the numerator. From Bartholomous et al. [5], we use the estimates

$$u_s \approx 1 \text{ m day}^{-1}, \quad A \approx 2.4 \times 10^{-24} \text{ s}^{-1} \text{ Pa}^{-n} \quad H \approx 500 \text{ m} \quad \text{and} \quad \Delta p \approx 1.80 \times 10^6 \text{ Pa},$$

which lead to a strain rate ratio of

$$S \approx 10^{-3}.$$

If we consider ice stream shear margins, the scaling for the strain rate ratio is similar except that the lengthscale L is now half the width of the

shear margin, so that

$$S \sim \frac{u_s}{AL\Delta p^n}.$$

Using estimates from Joughin et al. [24] and Perol and Rice [30] we have

$$u_s \approx 500 \text{ m yr}^{-1}, \quad A \approx 2.18 \times 10^{-24} \text{ s}^{-1} \text{ Pa}^{-n} \quad L \approx 3500 \text{ m} \quad \text{and} \quad \Delta p \approx 5 \times 10^5 \text{ Pa},$$

which leads to strain rate ratio of about

$$S \approx 10^{-2},$$

although, estimates in the range $S \sim 10^{-3}$ to $S \sim 1$ are reasonable for slightly different parameter values. For mountain glaciers, a similar range exists but is generally an order of magnitude smaller, i.e. $S \sim 10^{-4}$ to $S \sim 10^{-1}$.

4.3.2 NYE SOLUTION FOR A FINITE DOMAIN

Based on the estimates for S from mountain glaciers and ice streams, we consider the case when $S \ll 1$, i.e. when in-plane motion dominates antiplane shear. To first order in S we have that

$$T_E = \frac{1}{2} |\Sigma_{rr} - \Sigma_{\theta\theta}| \quad \text{and} \quad \dot{E}_E = |\dot{E}_{rr}|.$$

Since the problem is axisymmetric the in-plane shear stress is zero. Using mass conservation, we have

$$\dot{E}_{rr} + \dot{E}_{\theta\theta} = \frac{dU_r}{dR} + \frac{U_r}{R} = 0,$$

which is an ordinary differential equation for the velocity that we can integrate to give

$$U_r = -\frac{C}{R}.$$

This solution depends on the rheology only through the constant C . Taking the derivative of the radial velocity, we find that the effective strain rate is given as

$$\dot{E}_E = \frac{C}{R^2}.$$

Using the stress-strain rate relationship, equation (4.4), we can see that

$$\Sigma_{\theta\theta} - \Sigma_{rr} = 2\dot{E}_{\theta\theta}T_E^{1-n} = 2\dot{E}_{\theta\theta}\frac{T_E}{\dot{E}_E} = 2\dot{E}_{\theta\theta}\frac{\dot{E}_E^{1/n}}{\dot{E}_E} = -2\left(\frac{C}{R^2}\right)^{1/n}.$$

Now from a force balance we have

$$\frac{d\Sigma_{rr}}{dR} = \frac{\Sigma_{\theta\theta} - \Sigma_{rr}}{R} = -\frac{2C^{1/n}}{R^{2/n+1}}.$$

Integrating from $R = 1$ to $R = B$ gives

$$\int_1^B \frac{d\Sigma_{rr}}{dR} dR = -1 = \int_1^B \frac{2C^{1/n}}{R^{2/n+1}} dR = \left[\frac{nC^{1/n}}{R^{2/n}} \right]_1^B.$$

Solving for C we have that

$$C = n^{-n} \left(1 - \frac{1}{B^{2/n}} \right)^{-n},$$

which is positive for $n > 0$ and $B > 1$. Inserting it into the radial velocity we have

$$U_r = -\frac{n^{-n}}{R} \frac{B^2}{(B^{2/n} - 1)^n}, \quad (4.11)$$

which is the nondimensional Nye Solution for a finite domain. This equation can be compared to equation (4.1), which is the dimensional and infinite domain Nye solution.

4.4 RESULTS

4.4.1 PERTURBATION

ANTI-PLANE VELOCITY AND STRAIN RATES

Here we compute the perturbation antiplane velocity. At first order in S , the effective deviatoric stress and effective strain rate are given by the Nye solution and are only a function of R , i.e.

$$T_E = \left| \frac{C}{R^2} \frac{R^2}{|C|} \left(\frac{|C|}{R^2} \right)^{1/n} \right| = \frac{1}{nR^{2/n}} \left(1 - \frac{1}{B^{2/n}} \right)^{-1} \quad \text{and} \quad \dot{E}_E = \frac{n^{-n}}{R^2} \left(1 - \frac{1}{B^{2/n}} \right)^{-n}.$$

Now the stress can be related to the out of plane velocity as

$$(T_E)^{n-1} \Sigma_{rz} = \frac{1}{2} \frac{\partial U_z}{\partial R} \quad \text{and} \quad (T_E)^{n-1} \Sigma_{\theta z} = \frac{1}{2R} \frac{\partial U_z}{\partial \theta}.$$

Inserting this into the force balance we have

$$\frac{1}{R} \frac{\partial}{\partial R} \left[R (T_E)^{1-n} \frac{\partial U_z}{\partial R} \right] + \frac{(T_E)^{1-n}}{R^2} \frac{\partial^2 U_z}{\partial \theta^2} = 0.$$

We can then insert the effective stress to find

$$R^{(2/n)-1} \frac{\partial}{\partial R} \left(R^{3-2/n} \frac{\partial U_z}{\partial R} \right) + \frac{\partial^2 U_z}{\partial \theta^2} = 0. \quad (4.12)$$

This is an equidimensional, linear equation for the antiplane velocity U_z .

The boundary conditions for this equation are

$$\left. \frac{\partial U_z}{\partial R} \right|_{R=1} = 0 \quad \text{and} \quad U_z(R=B) = B \cos(\theta).$$

A method to solve equation (4.12) subject these boundary conditions is described in Appendix B.1. The solution for the antiplane velocity U_z is

$$U_z = B \frac{(R^{\lambda_+}/\lambda_+) - (R^{\lambda_-}/\lambda_-)}{(B^{\lambda_+}/\lambda_+) - (B^{\lambda_-}/\lambda_-)} \cos(\theta), \quad (4.13)$$

where λ_+ and λ_- are positive and negative solutions to the characteristic polynomial, equation (B.1) for $k = 1$. Equation (4.13) shows that points at the edge of the channel displace in the antiplane direction as if

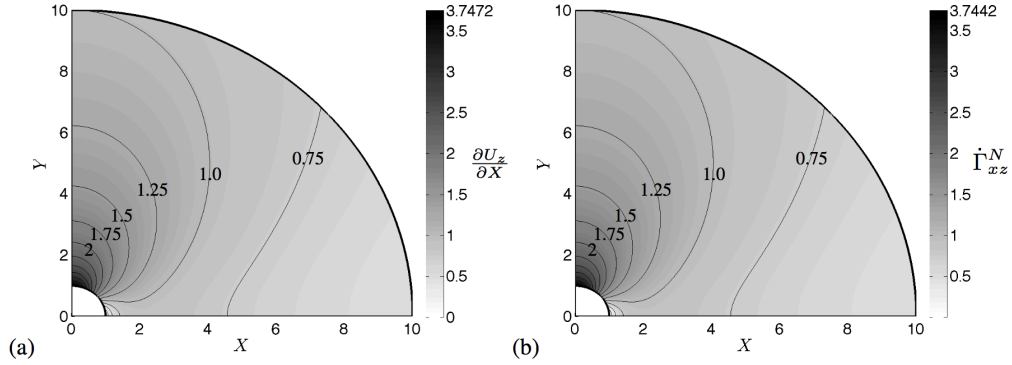


Figure 4.2: Horizontal antiplane strain rate $\partial U_z/\partial X$ (corresponding to dimensional $\dot{\gamma}_{xz}$) for $S \ll 1$, small antiplane perturbation of in-plane flow field: (a) analytical solution from for $\partial U_z/\partial X$, derivative of equation (4.13) and (b) the derivative of the numerical solution to equation (4.12), i.e. the nondimensional numerical strain rate $\dot{\Gamma}_{xz}^N$. The maximum value of horizontal strain rate, the strain rate concentration factor, $\xi_x = 3.7472\dots$ is located on the top of the channel. Black lines are drawn to denote the outer and inner edges of the domain in both figures.

the interior underwent a homogeneous deformation rate, which is similar to the results obtained by Eshelby [14]. The analytical derivative of equation (4.13), the horizontal strain rate, is plotted in figure 4.2(a). The actual expression for $\partial U_z/\partial X$ is omitted but can be computed from equation 4.13. Figure 4.2(b) shows the difference between the numerical strain rate $\dot{\gamma}_{xz}^N$ computed from the numerical solution to equation (4.12) and the analytical solution $\partial U_z/\partial X$.

For our numerical solutions, we used the existing numerical Finite Element Method (FEM) packages ABAQUS and COMSOL. In COMSOL, we developed a 2-dimensional plane-strain, steady state FEM model to solve for the perturbation solution, equation (4.12). To model the fully

coupled problems, where the ice viscosity is a function of both the in-plane and the antiplane components, we constructed an ABAQUS model using a thin (one element thick), transient, 3-dimensional FEM model constrained to deform by a combination of plane strain and antiplane strain. We coupled the displacements of the nodes on opposite faces of the geometry through the thickness to ensure that the model maintains a state of combined antiplane and plane strain. We generated the FEM mesh for both models using reduced integration isoparametric elements with significant refinement near the channel boundary. In order to validate both models, we compared numerical solutions to the known in-plane Nye solution without antiplane stresses. This numerical comparison yielded a nodal error of less than 0.8% for the ABAQUS simulations.

REGIME OF VALIDITY

As R increases toward the outer edge of the domain, the in-plane velocity decays as $1/R$, as per the Nye solution, equation (4.11). The antiplane velocity, however, is largest along the outer edge. Thus, for the perturbation solution to be valid throughout the domain, we require that along the line $\theta = 0$ and at the outer edge of the domain, $R = B$, the ratio of antiplane shear strain rate to the minimum in-plane strain rate, i.e.

$$\frac{\dot{\gamma}_{far}}{\dot{\epsilon}_{rr}(R=B)} = n^n S (B^{2/n} - 1)^n ,$$

is small. This gives a condition for validity, i.e.

$$n^n S (B^{2/n} - 1)^n \ll 1.$$

Rearranging this condition we find that the outer radius must satisfy

$$B_{cr} \ll \left(1 + \frac{1}{nS^{1/n}}\right)^{n/2}. \quad (4.14)$$

The outer radius must be larger than the inner radius, as both n and S are positive and the domain must be smaller for larger S . For $S = 10^{-3}$ and $n = 3$, we have that $B_{cr} \ll 10$ and, thus, this condition is violated as S approaches $S = 10^{-3}$, which is seen in figure 4.3.

4.4.2 STRAIN RATE CONCENTRATION FACTOR CHANGES WITH S

The strain rate concentration factor is an important parameter that is used to describe systems under shear. Here the dominant shear is antiplane, thus, the antiplane strain rate concentration factor ξ_i is the maximum value of strain rate in the direction i normalized by the loading strain rate, i.e.

$$\xi_i = \max \{\dot{\epsilon}_{iz}\} / (\dot{\gamma}_{far}/2) = \max \left\{ \frac{\partial u_z}{\partial x_i} \right\} / \dot{\gamma}_{far}.$$

Nondimensionalizing the velocity and spatial variables, the horizontal and vertical strain rate concentration factors ξ_x and ξ_y are given as

$$\xi_x = \max \left\{ \frac{\partial U_z}{\partial X} \right\} \quad \text{and} \quad \xi_y = \max \left\{ \frac{\partial U_z}{\partial Y} \right\}. \quad (4.15)$$

We now consider how the antiplane strain rate concentration factor for a finite domain ($B = 10$) depends on the strain rate ratio, S . In other words, as the amount of antiplane straining is increased in comparison to in-plane straining (i.e. as S increases), we can see in figure 4.3 that the value of the horizontal strain rate concentration factor ξ_x decreases. In the perturbation regime, i.e. when $S \ll 1$, the horizontal strain rate concentration factor is

$$\xi_x = \max \left\{ \frac{\partial U_z}{\partial X} \right\} = \frac{(B/\lambda_+) - (B/\lambda_-)}{(B^{\lambda_+}/\lambda_+) - (B^{\lambda_-}/\lambda_-)} = 3.7472 \dots \quad (4.16)$$

for $B = 10$, which is the maximum strain rate shown in figure 4.2. In the large S limit, analytical techniques proved ineffective and we must rely on numerical simulations. That is, with $n = 3$, our numerical simulations give that $\xi_x \approx 3.0768$. From our simulations we can also determine the horizontal strain rate concentration factor as a function of S , which is shown in figure 4.3. For small values of S , up to about $S = 10^{-3}$, the perturbation solution works, equation (4.16). From about $S = 1$ to higher values the fully antiplane solution prevails. In the region between these two limits, ξ_x decays quickly. This decay does not occur around $S = 1$, as

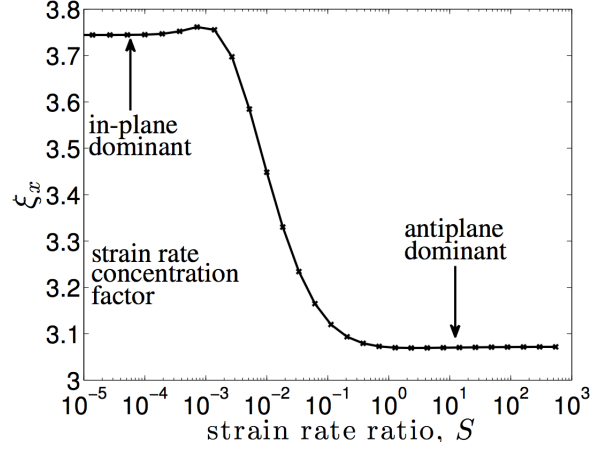


Figure 4.3: Horizontal strain rate concentration factor $\xi_x = \dot{\gamma}_{xz}/\dot{\gamma}_{far}$ as a function of the antiplane to in-plane strain rate ratio $S (= \dot{\gamma}_{far}/A\Delta p^n)$ for a finite domain with outer radius $B = 10$. This value is the maximum strain rate in the domain and occurs along the Y -axis on the top of the channel, i.e. at $(0, a)$. For small values of S , ξ_x is given by the perturbation solution. For large S , we see that ξ_x approaches the fully antiplane value $\xi_x \approx 3.0768$ for the finite domain.

one might expect, i.e. when the antiplane and in-plane strain rates are of similar order, but rather around $S = 10^{-2}$. The reason for this comes from the finite domain condition. As S increases, for the perturbation solution to remain valid, the domain size must decrease, as can be seen from equation (4.14). Here we keep a constant domain size, $B = 10$, and based on the regime of validity condition, equation (4.14), the solution is affected by the outer boundary around $S = 10^{-3}$. Furthermore, for a reasonable outer radius size ($B > 2$), this condition will dictate when antiplane dominates in-plane.

The antiplane strain rate concentration factor ξ_x is a useful param-

ter to describe antiplane motion for any value of S . Figure 4.3 shows the transition between the in-plane and antiplane dominated regimes. For large S , the strain rate concentration factors are also indicators of effective strain rate maxima. The horizontal strain rate concentration factor ξ_x is located at the top of the channel, where, because of symmetry the vertical strain rate must be zero. At this point, the effective strain rate \dot{E}_E is

$$\dot{E}_E = \sqrt{\dot{E}_{rr}^2 + \frac{1}{4}\xi_x^2},$$

and we can see that \dot{E}_E increases with ξ_x . Thus, as the effective strain rate increases, the prefactor in the rheology, equation (4.4), decreases, i.e. a shear-thinning rheology. We know that the highest strain rates in the system occur at the top of the channel, thus, the lowest viscosity also occurs at the top of the channel. The effective strain rates as a function of S are plotted in figure 4.4. For small S , the viscosity is dominated by the in-plane strain rates and as S increases, the effective strain rate levels off to a constant set by the horizontal antiplane strain rate concentration factor ξ_x . The curve for ξ_x as a function of S in figure 4.3 is also plotted on figure 4.4, but due to the small variation appears as essentially a flat line.

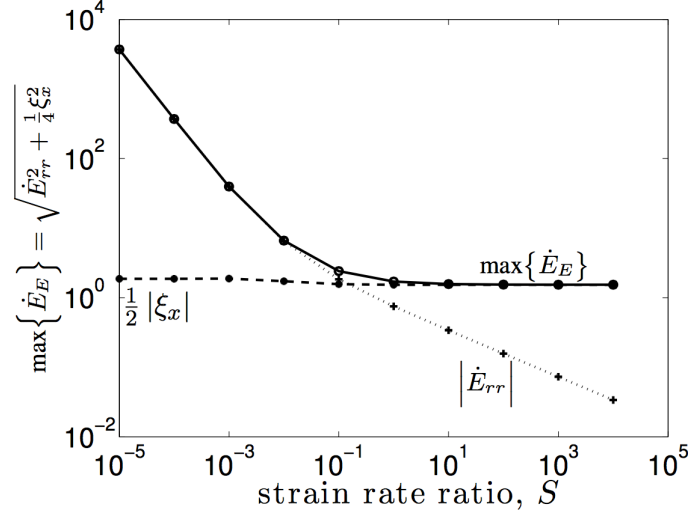


Figure 4.4: Numerical simulation results for the maximum effective strain rate and components \dot{E}_{rr} and $\xi_x/2$ as a function of S and evaluated at the top of the channel. The in-plane strain rate $\dot{E}_{rr} = \partial U_r / \partial R$ dominates for small S . The large S limit is given by the horizontal strain rate concentration factor $\xi_x = \partial U_z / \partial X$. The outer radius for these simulations is $B = 10$.

4.4.3 INFINITE DOMAIN

So far we have considered that there is a finite outer boundary of the domain located at $R = B$. For a finite domain, the outer boundary location B must satisfy a constraint in order for the perturbation solution to be valid. Now in the infinite domain, we can see from equation (4.1) that even without superimposed antiplane shear straining, the in-plane velocity decays as the radial coordinate R increases. If antiplane straining is then applied at $R = \infty$, we expect that there will be a region where the in-plane solution is small enough to no longer affect the viscosity and the antiplane components, although initially small, will be dominant. Thus,

for any value of the strain rate ratio S and distances much larger than a transition radius $R = \mathcal{R}$, which is a function of S , the solution will be antiplane dominated. A first guess for the transition radius \mathcal{R} can be seen from the effective strain rate \dot{E}_E . The in-plane strain rate \dot{E}_{rr} is given by the derivative of nondimensional Nye solution. Inserting this into the viscosity gives

$$\dot{E}_E = \sqrt{\frac{n^{-2n}}{R^4} + S^2 (\dot{E}_{rz}^2 + \dot{E}_{\theta z}^2)}. \quad (4.17)$$

Therefore, one would expect the transition radius to occur at

$$R \sim \mathcal{R} = \frac{1}{\sqrt{S}}, \quad (4.18)$$

as that is when the in-plane components in equation (4.17) are negligible and the viscosity is determined by the antiplane components. However, it turns out that equation (4.17) does not describe the viscosity near the transition radius (cf. figure 4.5) because the in-plane strain rates deviate from the Nye solution for even small S .

In order to evaluate the scaling in equation (4.18), we run numerical simulations. We find the antiplane velocity U_z as a function of R for many different values of S . One example, for $S = 10^{-3}$, is shown in figure 4.5(a). We expect that for small R the perturbation solution described in section 4.4.1 will be valid. For large R , we also expect that there will be a region of antiplane dominated velocity. The far field boundary con-

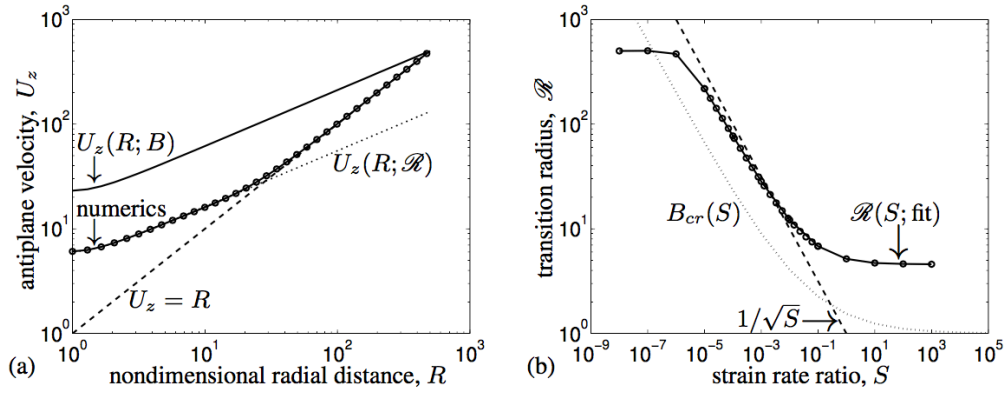


Figure 4.5: Small antiplane perturbations in an “infinite” domain: (a) antiplane velocity U_z , comparing the perturbation solution $U_z(R; B)$ equation (4.13), solid line, and numerical solution (circle line) for U_z as a function of R along $\theta = 0$ with $B = 500$, $n = 3$, and $S = 10^{-3}$. Perturbation solution fit to simulation, equation (4.20), $U_z(R; \mathcal{R})$, dotted line, and outer solution for large R , equation (4.19), $U_z = R$, dashed line, are also plotted. (b) Transition radius \mathcal{R} , as computed by the fit $U_z(R; \mathcal{R})$ in (a), called $\mathcal{R}(S; \text{fit})$, as a function of S (circle line). Simple scaling, equation (4.18), $\mathcal{R} \sim 1/\sqrt{S}$, dashed line, and regime of validity outer domain size, equation (4.14), $B_{cr}(S)$ with $n = 3$, dotted line.

dition is

$$U_z = R \cos(\theta), \quad (4.19)$$

and since this is a solution to the fully non-linear antiplane equations, we expect this to be the first term in the outer expansion for U_z .

Now we can see from figure 4.5(a) that the perturbation solution, equation (4.13), deviates considerably from the numerical simulations. The reason is that the outer boundary condition for equation (4.13) is applied at the edge of the domain. This is incorrect in this case because the outer edge of the domain is outside the region of validity for the perturbation solution. Thus, the outer boundary for the perturbation solution should be applied at the transition radius $R = \mathcal{R}$ rather than at $R = B$. Since the shape of the perturbation solution looks correct, we do a one-point fit to the numerics to determine the transition radius \mathcal{R} through

$$U_z = \mathcal{R} \frac{(R^{\lambda_+}/\lambda_+) - (R^{\lambda_-}/\lambda_-)}{(\mathcal{R}^{\lambda_+}/\lambda_+) - (\mathcal{R}^{\lambda_-}/\lambda_-)} \cos(\theta). \quad (4.20)$$

We then plot the transition radius \mathcal{R} as a function of S in figure 4.5(b). This figure shows that the simple scaling described in equation (4.18) is flawed. The values predicted from the simple scaling are close to correct for strain rate ratios around $S = 10^{-3}$ but the slope is not correct and there are significant deviations for smaller values of S . Another candidate for the scaling of the outer boundary location is the regime of validity curve determined in section 4.4.1. If the condition in equa-

tion (4.14) is satisfied, then the perturbation solution will be valid up to that distance. This estimate for the transition radius is more conservative and decays to unity for large S , although, the slope is closer to agreement with the numeric results. The transition radius, as computed from the one-point fit in equation (4.20), does not decay to unity for S but rather decays to a finite value. This comes from the fact that as S increases, the antiplane velocity U_z approaches the solution for the fully antiplane problem, which differs from the far-field condition, equation (4.19), near the channel. The shape of U_z also deviates from the perturbation solution with the transition radius \mathcal{R} as the far field boundary, equation (4.20). Thus, as S increases and the antiplane velocity approaches the fully antiplane solution, the apparent value of the transition radius, computed from the fit in equation (4.20), also asymptotes to a constant value.

Figure 4.5 shows that the simple scaling $\mathcal{R} \sim 1/\sqrt{S}$ does not accurately predict the radius at which the dominant deformation mechanism transitions from in-plane to antiplane. The argument behind this scaling is one of intermediate asymptotics, i.e. there is some intermediate range of S , where both deformation mechanisms exist within the domain [4]. The problem is that the Nye solution, which is used in equation (4.17) to account for the in-plane strain rates, is only valid for $S \ll 1$. This can be seen graphically in figure 4.4. In the intermediate asymptotic region, $10^{-6} < S < 10^{-2}$, the small amount of antiplane shear is non-negligible

in the in-plane strain rates and there is a nonlinear feedback through the viscosity. Thus, for S in the range $10^{-6} < S < 10^{-2}$, we do not have a closed form solution for the in-plane strainrates, which makes it difficult to give a scaling for the transition radius \mathcal{R} .

A similar scaling to equation (4.18) is derived in Weertman [45] to represent the transition between in-plane and antiplane dominated regions. The problem that Weertman [45] examined is antiplane shear traction applied along the glacier base outside of a Röthlisberger channel. Weertman [45] finds the transition radius, $\mathcal{R} \sim (\Delta p / \tau)^{n/2}$. This scaling can also be written as $\mathcal{R} \sim (1/S)^{n/2}$, where we define S as $\tau / \Delta p$. Our analysis shows, however, that the simple scaling cannot predict the transition between in-plane dominated and antiplane dominated creep. Thus, we expect that the transition radius given in Weertman [45] falls into the same intermediate asymptotic as the scaling we derived and, therefore, will also give incorrect predictions. We are currently working on numerical simulations of the Weertman [45] problem in order to evaluate his analysis. For example, Weertman [45] also uses the simple scaling to compute a distance at which water can be pulled into the Röthlisberger channel. However, this analysis requires a hydrologic model in the region outside the channel. In this case, the antiplane shear becomes a function of the pore pressure and coupled the deformation with hydrology, much like Perol et al. [31]. This research is currently in progress, cf. Fernandes et al. [15].

4.4.4 LARGE PERTURBATIONS

Here we consider very large values of S , i.e. $S \gg 1$, which occur when antiplane shear strain rate strongly dominates the in-plane strain rate. In the limit of very large S , the (nondimensional) effective stress and strain rate, from equation (4.3), reduce to

$$T_E = S\sqrt{\Sigma_{rz}^2 + \Sigma_{\theta z}^2} \quad \text{and} \quad \dot{E}_E = S\sqrt{\dot{E}_{rz}^2 + \dot{E}_{\theta z}^2}. \quad (4.21)$$

Before, in the small S limit, the Nye solution for the in-plane velocity set the effective viscosity. Here we have the opposite limit and the effective viscosity of the ice is set by the antiplane motion. Thus, the in-plane velocity no longer influences the effective viscosity. In this regime, the nonlinearity of the equations in the in-plane direction disappears and the channel will close like a Newtonian ($n = 1$) fluid with a spatially variable viscosity. Here we seek to determine how the creep closure velocity U_r depends on S .

From mass conservation we have

$$\frac{\partial U_r}{\partial R} + \frac{U_r}{R} + \frac{1}{R} \frac{\partial U_\theta}{\partial \theta} = 0.$$

To avoid the θ dependence in our results, we examine quantities that are

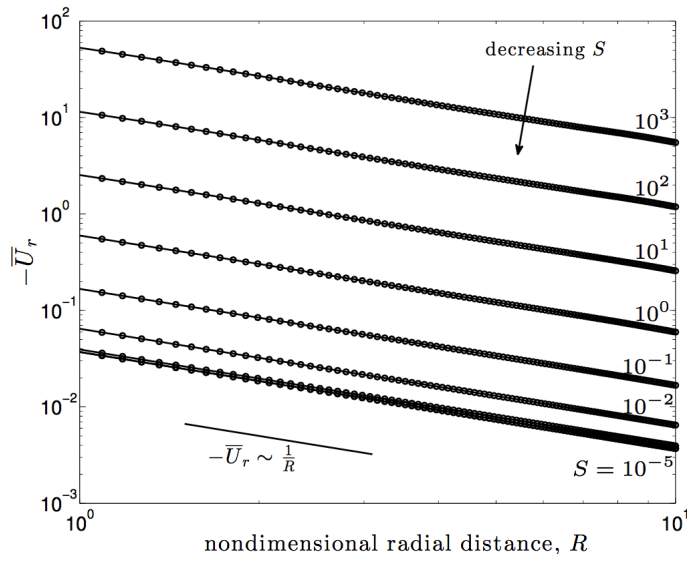


Figure 4.6: Average creep closure (radial velocity) $-\bar{U}_r$ as a function of R . The range of S is from $S = 10^{-5}$ (bottom circle line) to $S = 10^3$ (top circle line) in powers of ten. For all values of S , the average creep closure decays as $1/R$ (solid line). For small S , the creep closure asymptotes to the Nye solution. The outer radius for these simulations is $B = 10$.

averaged over $\theta \in [0, 2\pi]$, noting that

$$\overline{U}_r = \frac{1}{2\pi} \int_0^{2\pi} U_r d\theta \quad \text{and} \quad \frac{1}{2\pi} \int_0^{2\pi} \frac{\partial U_\theta}{\partial \theta} d\theta = 0.$$

Thus, mass conservation can be written as

$$\frac{\partial \overline{U}_r}{\partial R} + \frac{\overline{U}_r}{R} = 0,$$

and we can write the solution \overline{U}_r in the form,

$$\overline{U}_r = -\frac{C}{R}, \tag{4.22}$$

which agrees with numerical simulations, see figure 4.6. Furthermore, for $S = 0$, the average creep closure velocity is equal to the axisymmetric Nye solution, equation (4.1). Thus, all we are looking for is the S dependence of C in equation (4.22).

Now the in-plane rheology is given as

$$\dot{E}_{rr} = \frac{1}{2} T_E^{n-1} (\Sigma_{rr} - \Sigma_{\theta\theta}).$$

Using equation (4.21), we can see that

$$\dot{E}_{rr} = \frac{1}{2} S^{\frac{n-1}{n}} (\dot{E}_{rz}^2 + \dot{E}_{\theta z}^2)^{\frac{n-1}{2n}} (\Sigma_{rr} - \Sigma_{\theta\theta}). \tag{4.23}$$

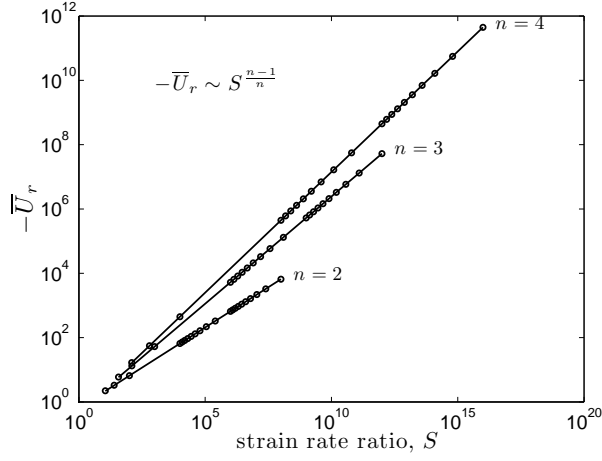


Figure 4.7: Average creep closure (radial velocity) $-\bar{U}_r$ at $R = 1$ scaling for large S . The outer radius for these simulations is $B = 10$.

The in-plane strain rate scales with the in-plane velocity as

$$\dot{E}_{rr} \sim -\dot{E}_{\theta\theta} \sim -\frac{\bar{U}_r}{R},$$

and inserting the strain rate scaling into equation (4.23) at $R = 1$ gives the scaling

$$-\bar{U}_r \sim S^{\frac{n-1}{n}},$$

which can be seen in figure 4.7 for three different values of n and $B = 10$. A more detailed derivation of this scaling relationship is derived in Appendix B.2.

4.5 IMPLICATIONS FOR RÖTHLISBERGER ANALYSIS

Here we outline the standard Röthlisberger analysis and combine our analysis above for the different regimes in S to describe how the channel diameter changes as a function of S . We also discuss how the assumption of axisymmetry breaks down as S increases leading to a discussion of non-circular channels. In the standard analysis, Röthlisberger channels are modelled as turbulent pipes with circular cross section. The Manning-Strickler equation for a turbulent flow in a rough-walled pipe is given as

$$Q = \frac{A_c R_h^{2/3} \sin^{1/2}(\alpha)}{n_m},$$

where n_m [$\text{s m}^{-1/3}$] is the Gauckler-Manning roughness coefficient, Q is the fluid flow rate, $\sin(\alpha)$ is the slope, A_c is the cross sectional area and R_h is the hydraulic radius, which is defined as $R_h \equiv A_c/P_r$ for the wetted perimeter P_r . We can write the flow rate as a function of the circular channel diameter D as

$$Q = \frac{\pi D^{8/3} \sin^{1/2}(\alpha)}{2^{10/3} n_m}. \quad (4.24)$$

In the Röthlisberger channel analysis, the water and ice are assumed to be at the melting temperature [35]. Thus, all of the energy generated by the turbulent flow goes into melting at the channel walls. In steady state

we can write

$$\pi \rho_{ice} \mathcal{L} D u_{melt} = \rho_w g \sin(\alpha) Q, \quad (4.25)$$

for ice density ρ_{ice} , water density ρ_w , and latent heat per unit mass \mathcal{L} [45]. In equilibrium, the melt velocity u_{melt} is equated to the average creep closure rate, $\bar{u}_{cr} = |\bar{u}_r(r = a)|$ in absolute value, which comes from our simulations. We use the average to ensure that the creep closure maintains the axisymmetry as S increases. The diameter of the Röthlisberger channel is found by inserting Q from equation (4.24) into equation (4.25) and solving for D , using the fact that u_{melt} is the same as \bar{u}_{cr} . This gives

$$D = 4 \left(\frac{\rho_{ice} \mathcal{L}}{\rho_w g} \frac{\bar{u}_{cr} n_m}{\sin^{3/2}(\alpha)} \right)^{3/5}. \quad (4.26)$$

We find \bar{u}_{cr} as a function of Δp from ABAQUS simulations and use \bar{u}_{cr} to compute D . We set a single value for the pressure difference and calculate the far-field strain rate required to give the value of S . The value chosen (see table 4.1) is similar to pressure difference found in Perol et al. [31] for the Siple Coast ice streams.

An important feature to notice about the Röthlisberger analysis is that the diameter D and the flow rate Q are coupled by equation (4.24), the Manning-Strickler equation, which is independent of the pressure difference Δp . This means that a fixed Δp gives the diameter D and simul-

taneously the flow rate Q through the Manning-Strickler equation. We could also specify a channel diameter (or flow rate) and then compute the required pressure difference, which is what is done in Perol et al. [31]. In our simulations, it is easier to set Δp and use the creep closure from the simulations to compute D and Q because \bar{u}_{cr} is an unknown function of the pressure difference. However, if a flow rate was specified, as an estimate from a subglacial hydrology model or observational estimates, the diameter could be computed from equation (4.24) and then the melt rate u_{melt} would be specified through equation (4.25). Then in our finite element simulations, we would know the size of the channel and would have to shoot for the value of Δp such that the value of \bar{u}_{cr} at the edge of the channel is equal to u_{melt} given from equation (4.25).

4.5.1 NON-CIRCULAR RÖTHLISBERGER CHANNELS

When the superimposed antiplane strain rate increases with respect to the in-plane strain rate, i.e. as S increases, the solution is no longer axisymmetric and thus, u_r is averaged over the arc of the circle to get rid of the θ dependence. This treatment ignores the possibility that under large amounts of antiplane strain the channel shape will deviate from circular. The simulations show that the creep closure velocity increases on the top of the channel (i.e. along y axis of figure 4.1) and decreases on the sides (along x axis) relative to the average creep closure velocity \bar{u}_{cr} . This follows from the fact that the minimum viscosity, as shown in

section 4.4.2, occurs at the top of the channel. Using a uniform meltrate, circular channels would deform and be melted into channels that are wider than they are tall. Observational evidence shows that channels often do become wider than tall [16]. The difference is that in our simulations, the antiplane deformation is lateral and we have assumed that in mountain glaciers the predominant straining is vertical. Thus, our simulations are still relevant: the results just need to be rotated ninety degrees. This would indicate that in mountain glaciers, with vertical antiplane shear, our simulations predict channels that are taller than wide, which is contrary to the observations. In ice streams and near the side-walls of mountain glaciers, the antiplane shear straining is along the axis of the channel and our predictions are in agreement with the observations.

Dallaston and Hewitt [9] show that circular channels under axisymmetric in-plane loading with a constant meltrate M are unstable to linear perturbations for both shear-thinning and Newtonian viscosities. In the Newtonian fluid case, this instability can be stabilised by the addition of a uniform heat source that diffuses to the free boundary of the channel where a Stefan condition is applied. The linear problem (i.e. Newtonian, $n = 1$) is tractable analytically and circular channels are shown to be stable for all wavemodes, except the lowest, which is neutrally stable and perturbs the circular channel to an elliptical channel. The steady-state for an elliptical channel is dependent on its aspect ratio, where larger

ρ_{ice}	910	$[\text{kg m}^{-3}]$	ice density
ρ_w	1000	$[\text{kg m}^{-3}]$	water density
g	9.8	$[\text{m s}^{-2}]$	gravity
\mathcal{L}	333,500	$[\text{m}^2 \text{s}^{-2}]$	latent heat
n_m	0.025	$[\text{s m}^{-\frac{1}{3}}]$	Manning coefficient
$\sin(\alpha)$	0.001	$[-]$	surface slope
A	2.18×10^{-24}	$[\text{s}^{-1} \text{Pa}^{-n}]$	ice softness
n	3	$[-]$	rheological power
Δp	5×10^5	$[\text{Pa}]$	pressure difference

Table 4.1: Parameters similar to those from Siple Coast ice streams [31].

aspect ratios are more stable. Much of this insight should carry over to the shear-thinning fluid with uniform melting coupled at the channel surface free boundary by a Stefan condition. Thus, it is expected that circular channels in a shear-thinning fluid can be stabilised by the melting from the temperature field. This could be confirmed using finite element simulations, as the boundary element method employed in Dallaston and Hewitt [9] does not work for shear-thinning fluids. In these finite element simulations, it would also be worth considering the more realistic heat transfer imparted by the turbulently flowing melt-water rather than the temperature field around a uniform heat source. These simulations would provide great insight into the shape and stability of R  thlisberger channels.

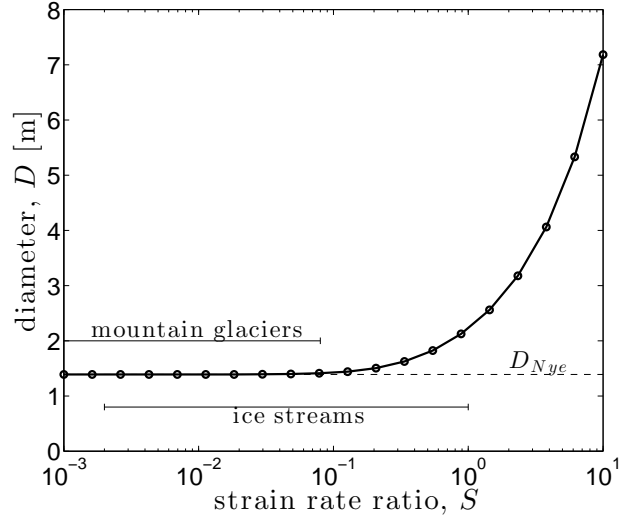


Figure 4.8: R  thlisberger channel diameter as a function of the antiplane to in-plane strain rate ratio S . The finite domain effects are scaled out. Representative ranges of S for ice streams and mountain glaciers are based on parameters from section 4.3.1 and table 4.1.

4.5.2 R  THLISBERGER CHANNEL DIAMETER WITH S

For the small perturbation case, e.g. $S \ll 1$, there is no change to the standard R  thlisberger analysis. Using the Nye solution, equation (4.1), we can insert the parameters from table 4.1 and find that

$$D_{Nye} = \left(\frac{2^{7/3} \rho_{ice} \mathcal{L}}{n^n \rho_w g} \frac{A \Delta p^n n_m}{\sin^{3/2}(\alpha)} \right)^{3/2} \approx 1.39 \text{ m}.$$

This is consistent with Vogel et al. [43], who show flowing water with a depth of 1.6 meters at the base of the dormant Kamb ice stream shear margin. Figure 4.8 shows that for $S \lesssim 10^{-1}$, the Nye solution holds and the predicted channel size is exactly that found above. As S increases, it

leaves the small perturbation range and, thus, we cannot give the value for the diameter analytically. Numerically we find that for $S \sim O(1)$, the diameter roughly doubles in size. For very large S , which might be rare in mountain glaciers and ice streams, we can use the scaling from section 4.4.4 to show that the diameter of the channel should scale as $D \sim \bar{u}_{cr}^{3/2} \sim S^{3(n-1)/2n}$. As S increases the Röthlisberger channel size increases. This can be seen from equation(4.26): for a constant Δp , if \bar{u}_{cr} increases then D must also increase.

4.6 CONCLUSION

Antiplane shear can affect the in-plane creep closure of a Röthlisberger channel. A small perturbation in $S = \dot{\gamma}_{far}/A\Delta p^n$ removes antiplane motion from the effective viscosity and yields no effect on the creep closure of the Röthlisberger channel. With the ice viscosity set by the in-plane Nye solution ($S \ll 1$), we find a analytical solution for the antiplane velocity U_z . In a finite domain, the outer radius must satisfy an inequality or else there is a transition to an antiplane dominated regime near the edge of the domain. This is discussed further by examining the infinite domain, where there is a transition between in-plane dominated and antiplane dominated at some transition radius \mathcal{R} . We describe the inner and outer solutions that form as an intermediate asymptotic in S . For very large perturbations, the entire domain is antiplane dominant and we derive a scaling for the average creep closure as a function of S . We

use the strain rate concentration factor as a method quantifying local deformation as a function of S and numerically show two regimes: in-plane dominant and antiplane dominant. Our analysis culminates with the insight that small amounts of antiplane shear ($S \ll 1$) have no effect on the R  thlisberger channel size, but even moderate amounts ($S \sim 1$) of antiplane motion can double the diameter of the R  thlisberger channel.

5

Conclusion

The aim of this thesis has been to study the mechanics of subglacial hydrology under supraglacial lakes and in ice stream shear margins. For detailed conclusions, refer to the conclusion section of each chapter, as for this chapter I will cover the main ideas, learning experience and possible further extensions.

For the first part of the thesis, with regards to the project analyzing the creep opening of a crack crevasse under a supraglacial lake, we were able to obtain the profile for the opening of a crack crevasse under a supraglacial lake by using a FEM model of a crack in an infinite power law creep material. Comparing the numerical model's results to the time scales for the opening of the channel in chapter 3, we saw close agreement with data obtained from supraglacial lakes in the Western Greenland Ice Sheet. However, the model does not incorporate effects from a no slip boundary condition between the ice and the bed. Therefore, this model can be improved by a 3 dimensional finite element model, formulated as a plane strain problem, that takes into account a uniform shear stress across the thickness.

For the second part of the thesis, with regards to the project looking at the effects of antiplane strain rates superposed to the in-plane Röthlisberger channel analysis, we were able to derive analytical perturbation expressions for the channel with superimposed antiplane strain rates. We were also able to develop a FEM model for the opening of the channel and were ultimately able to compute the steady state diameter of the channel for various magnitudes of antiplane strain rates. However, this model assumes a channel that is fully incised in the ice sheet, where in ice stream shear margins it is conjectured that these channels will be formed along the ice-bed interface and that they will be locked on one side. Therefore, this model could be improved by looking at a semi-

circular channel model that takes into account the locking of the bed on one side.



Additional Material for Chapter 2

A.1 NYE SOLUTION FOR A FINITE BODY

Assuming a creep flow law of

$$\dot{\epsilon}_E = A\tau_E^n \quad (\text{A.1})$$

and incompressibility denoted by

$$\dot{\epsilon}_{11} + \dot{\epsilon}_{22} + \dot{\epsilon}_{33} = 0 \quad (\text{A.2})$$

this section derives the radial opening rate (\dot{u}_r) of a channel incised in a finite circular domain, with a geometry analogous to an annulus. In Cartesian coordinates we define the strain rate to be

$$\dot{\epsilon}_{ij} = \frac{1}{2} \left(\frac{\partial \dot{u}_i}{\partial x_j} + \frac{\partial \dot{u}_j}{\partial x_i} \right) \quad (\text{A.3})$$

where \dot{u}_i denotes the i component of the velocity. The shear equivalent strain (equivalent denoting the second invariant) rate is defined as

$$\dot{\epsilon}_E = \sqrt{\frac{1}{2} \dot{\epsilon}'_{ij} \dot{\epsilon}'_{ij}}, \quad (\text{A.4})$$

where $\dot{\epsilon}'_{ij}$ is the deviatoric strain rate given by

$$\dot{\epsilon}'_{ij} = \dot{\epsilon}_{ij} - \frac{1}{3} \dot{\epsilon}_{kk} \delta_{ij}. \quad (\text{A.5})$$

However due to the incompressibility constraint eq. (A.2) the second term of eq. (A.5) is 0. Thus, we can simplify eq. (A.4) as

$$\dot{\epsilon}_E = \sqrt{\frac{1}{2} \dot{\epsilon}_{ij} \dot{\epsilon}_{ij}}. \quad (\text{A.6})$$

Similarly, the equivalent (equivalent denoting the second invariant) shear stress is defined as

$$\tau_E = \sqrt{\frac{1}{2}s_{ij}s_{ij}} \quad (\text{A.7})$$

where s_{ij} is the deviatoric stress given by

$$s_{ij} = \sigma_{ij} - \frac{1}{3}\sigma_{kk}\delta_{ij}. \quad (\text{A.8})$$

Assuming a plane, axially symmetric flow, implies

$$\dot{\epsilon}_{zz} = 0 \text{ where } s_{zz} = 0. \quad (\text{A.9})$$

Therefore, from incompressibility we also know that gathering eqs. (A.1), (A.6), and (A.7), we can derive an expression for the (i,j) strain rate component as

$$\dot{\epsilon}_{ij} = \frac{\dot{\epsilon}_E}{\tau_E}s_{ij} = A\tau_E^{n-1}s_{ij}. \quad (\text{A.10})$$

The axially symmetric components of the deviatoric stress then become

$$s_{rr} = \frac{2\sigma_{rr} - \sigma_{\theta\theta} - \sigma_{zz}}{3} \quad (\text{A.11})$$

$$s_{\theta\theta} = \frac{2\sigma_{\theta\theta} - \sigma_{rr} - \sigma_{zz}}{3} \quad (\text{A.12})$$

$$s_{zz} = 0 = \frac{2\sigma_{zz} - \sigma_{\theta\theta} - \sigma_{rr}}{3} \Rightarrow \sigma_{zz} = \frac{1}{2}(\sigma_{\theta\theta} + \sigma_{rr}). \quad (\text{A.13})$$

Therefore we rewrite eq. (A.11) and eq. (A.12) as

$$s_{\theta\theta} = -s_{rr} = \frac{1}{2}(\sigma_{\theta\theta} - \sigma_{rr}). \quad (\text{A.14})$$

Since $s_{ij} = 0$ for $i \neq j$, we can simplify eq. (A.7) as

$$\tau_E = \sqrt{\frac{1}{2}(s_{rr}^2 + s_{\theta\theta}^2)} = |s_{\theta\theta}| = \frac{1}{2}|\sigma_{\theta\theta} - \sigma_{rr}|. \quad (\text{A.15})$$

The material model and incompressibility then gives us the following relation between the strain rate and velocity:

$$\dot{\epsilon}_{rr} = \frac{du}{dr}, \quad \dot{\epsilon}_{\theta\theta} = \frac{\dot{u}}{r} \quad (\text{A.16})$$

$$\dot{\epsilon}_{rr} + \dot{\epsilon}_{\theta\theta} = 0. \quad (\text{A.17})$$

Eq. (A.16) and eq. (A.17) imply that the radial velocity \dot{u} must take form of

$$\dot{u} = \frac{C}{r}. \quad (\text{A.18})$$

In the equilibrium equations we can cancel the shear components as they will be 0, thus yielding

$$\frac{d\sigma_{rr}}{dr} + \frac{\sigma_{rr} - \sigma_{\theta\theta}}{r} = 0. \quad (\text{A.19})$$

From eq. (A.14) we know that

$$\sigma_{\theta\theta} - \sigma_{rr} = 2s_{\theta\theta}, \quad (\text{A.20})$$

and from incompressibility we know that $\dot{\epsilon}_{\theta\theta} = -\dot{\epsilon}_{rr}$, so we can rewrite the equivalent strain rate as

$$\dot{\epsilon}_E = \sqrt{\frac{1}{2}(\dot{\epsilon}_{rr}^2 + \dot{\epsilon}_{\theta\theta}^2)} = |\dot{\epsilon}_{\theta\theta}| = \left| \frac{\dot{u}}{r} \right| = \frac{|C|}{r^2}. \quad (\text{A.21})$$

Using equation eq. (A.20) and eq. (A.21), we can write

$$\sigma_{rr} - \sigma_{\theta\theta} = -2s_{\theta\theta} = -2\dot{\epsilon}_{\theta\theta} \frac{\tau_E}{\dot{\epsilon}_E} \quad (\text{A.22})$$

as

$$\sigma_{rr} - \sigma_{\theta\theta} = -2\dot{\epsilon}_{\theta\theta} \frac{\left(\frac{\dot{\epsilon}_E}{A}\right)^{\frac{1}{n}}}{\dot{\epsilon}_E} = -2\frac{C}{r^2} \frac{1}{\frac{|C|}{r^2}} \left(\frac{|C|}{r^2 A}\right)^{\frac{1}{n}} = -2\frac{C}{|C|} \left(\frac{|C|}{A}\right)^{\frac{1}{n}} \left(\frac{1}{r^2}\right)^{\frac{1}{n}}. \quad (\text{A.23})$$

The equilibrium eq. (A.19) then becomes

$$\frac{d\sigma_{rr}}{dr} = \frac{\sigma_{\theta\theta} - \sigma_{rr}}{r} = 2\frac{C}{|C|} \left(\frac{|C|}{A}\right)^{\frac{1}{n}} \left(\frac{1}{r^{1+2/n}}\right). \quad (\text{A.24})$$

To find the solution we integrate the left hand side of eq. (A.24) and apply boundary conditions as

$$\int_a^R \frac{d\sigma_{rr}}{dr} = \sigma_{rr} \Big|_R - \sigma_{rr} \Big|_a = (-p_R) - (-p_a) = p_a - p_R, \quad (\text{A.25})$$

where a is the radius of the channel, R is the outer radius of the domain, p_a is the normal pressure in the channel and p_R is the outward normal pressure at the outer domain boundary. Combining eq. (A.25) and the integral of the right hand side of eq. (A.24) we see that

$$p_a - p_R = 2 \int_a^R \frac{C}{|C|} \left(\frac{|C|}{A} \right)^{\frac{1}{n}} \left(\frac{dr}{r^{1+2/n}} \right) = 2 \frac{C}{|C|} \left(\frac{|C|}{A} \right)^{\frac{1}{n}} \int_a^R \left(\frac{dr}{r^{1+2/n}} \right). \quad (\text{A.26})$$

Where the integration becomes

$$\int_a^R \frac{dr}{r^{1+2/n}} = -\frac{1}{2}n \left(\frac{1}{R^{2/n}} - \frac{1}{a^{2/n}} \right). \quad (\text{A.27})$$

Putting eq. (A.27) back into eq. (A.26) we get

$$p_a - p_R = 2 \frac{C}{|C|} \left(\frac{|C|}{A} \right)^{\frac{1}{n}} \frac{1}{2}n \left(\frac{1}{a^{2/n}} - \frac{1}{R^{2/n}} \right). \quad (\text{A.28})$$

Rearranging eq. (A.28) we get that C must be

$$C = A \left(\frac{p_a - p_R}{n} \right)^n \left(\frac{1}{a^{-2/n} - R^{-2/n}} \right)^n. \quad (\text{A.29})$$

Since the radial velocity was obtained as $\dot{u} = \frac{C}{r}$, we can finally arrive at the Nye solution for a finite domain given by

$$\dot{u}_r = \frac{A}{r} \left(\frac{p_a - p_R}{n} \right)^n \left(\frac{1}{a^{-2/n} - R^{-2/n}} \right)^n. \quad (\text{A.30})$$

Comparing this to the infinite Nye solution, where $R \rightarrow \infty$ by nondimensionalizing the opening rate by Nye's solution and the length scales by the inner radius a , we obtain that the nondimensional finite Nye solution is given by

$$\dot{U}_r(r) = \frac{a}{r} \left(\frac{1}{1 - \left(\frac{a}{R}\right)^{2/n}} \right)^n \text{ for } 0 < r < R. \quad (\text{A.31})$$

Since this scaling is independent of the creep stiffness coefficient A , we can factor in the correction accounting for the finiteness of the domain through A such that

$$A^* = A \left(a^{-2/n} - R^{-2/n} \right), \quad (\text{A.32})$$

where A^* is the corrected value for the creep stiffness coefficient used in the numerical model, a is the inner radius (or equivalently crack length for approximation) and R is the outer domain radius.

A.2 ALTERNATE DERIVATION OF OPENING RATE APPROXIMATION

Suppose a linear viscous material with an ellipsoidal cavity of major radius a and minor radius b undergoes a far-field uniaxial tension (σ_∞), in the direction of its minor axis (denoted by the y direction), as illustrated in fig. A.1. The known stress concentration solution relates

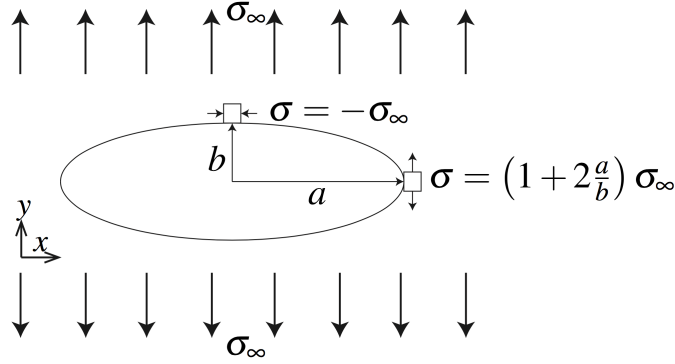


Figure A.1: Uniaxial far-field stress applied in the y-direction. Respective stress concentration factor is given at the given locations of the ellipse. Because of symmetry, the stress concentration factors also applies to the other side of the ellipse along the same axis.

the stress at the tip of major axis a to the far-field applied stress to be $\sigma = (1 + 2\frac{a}{b}) \sigma_{\infty}$ and at the tip of minor axis b to be $\sigma = -\sigma_{\infty}$.

Similarly, if we apply a far-field uniaxial tension in the orthogonal direction, such that we are pulling in the direction of the major axis a , then we can also relate the stress at the tip of minor axis b as $\sigma = (1 + 2\frac{b}{a}) \sigma_{\infty}$ and at the tip of the major axis a to be $\sigma = -\sigma_{\infty}$, as illustrated in fig. A.2

In a medium with a linear viscous constitutive model, we can superimpose these two solutions to achieve a hoop stress solution for an ellipsoidal cavity undergoing hydrostatic far-field stress σ_{∞} , as presented in fig. A.3. Using these solutions, the strain rate everywhere in the cavity can be achieved by

$$\dot{\epsilon}_y = \frac{2}{E'} \frac{a}{b} \sigma_{\infty} = \frac{\partial \dot{u}_y}{\partial y} \quad (\text{A.33})$$

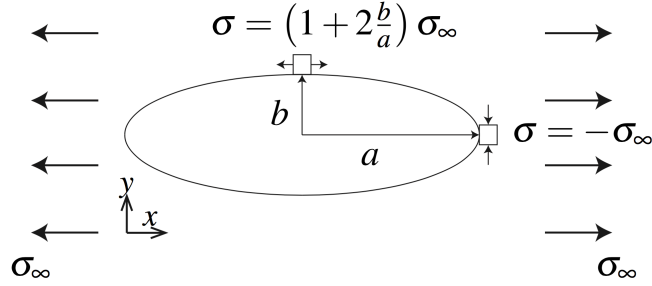


Figure A.2: Uniaxial far-field stress applied in the x-direction. Respective stress concentration factor is given at the given locations of the ellipse. Because of symmetry, the stress concentration factors also applies to the other side of the ellipse along the same axis.

and

$$\dot{\epsilon}_x = \frac{2}{E'} \frac{b}{a} \sigma_\infty = \frac{\partial \dot{u}_x}{\partial x}. \quad (\text{A.34})$$

Thus the opening rates can be derived for the linear case to be

$$\dot{u}_x = \frac{2}{E'} \frac{a}{b} x \quad (\text{A.35})$$

and

$$\dot{u}_y = \frac{2}{E'} \frac{a}{b} y. \quad (\text{A.36})$$

Using the nondimensional Cartesian ellipse equation $\frac{x^2}{a^2} + \frac{y^2}{b^2} = 1$ we can solve for the location along the boundary of the channel to be $y = b\sqrt{1 - \frac{x^2}{a^2}}$, such that we can get the channel opening rate as a function of x to be

$$\dot{u}_y = \frac{2}{E'} \frac{a}{b} b \sqrt{1 - \frac{x^2}{a^2}}. \quad (\text{A.37})$$

Where the effective plain strain youngs modulus is $E' = \frac{E}{1-\nu^2} = \frac{E}{1+\nu} \frac{1}{1-\nu} =$

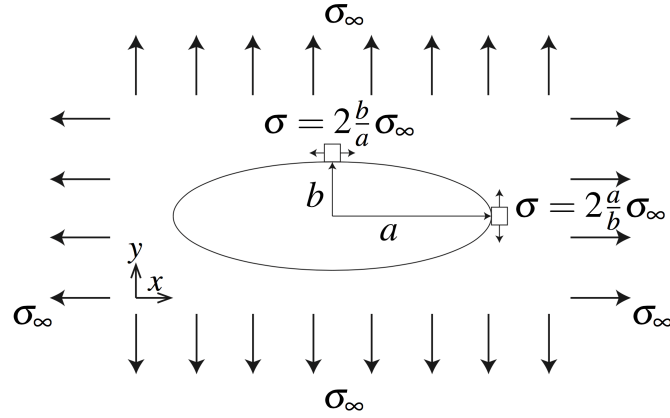


Figure A.3: Stress concentration factors solution for hydrostatic tension can be achieved by the superposition of solution in fig. A.1 and fig. A.2. The superposition principle can only be used for a problem using a linear constitutive model, such as a linear creep material.

$2G_{0.5}^{\frac{1}{2}} = 4G$. We can now rewrite eq. (A.37) as

$$\dot{u}_y = \frac{a}{2G} \sqrt{1 - \frac{x^2}{a^2}}. \quad (\text{A.38})$$

Replacing the elastic modulus with a linear power law creep material stiffness ($n=1$), where $\frac{1}{2G} \rightarrow \frac{\dot{\gamma}}{2} = \frac{\tau}{2\mu} = A\tau$, we obtain the that y-opening of the linear crack is given by

$$\dot{u}_y = A\tau a \sqrt{1 - \left(\frac{x}{a}\right)^2}. \quad (\text{A.39})$$

B

Additional Material for Chapter 4

B.1 METHOD FOR SOLVING ANTI-PLANE SOLUTION

Equation (4.12) is a linear, equidimensional equation. We therefore try for a solution of the form

$$U_z = R^\lambda f(\theta).$$

Inserting this ansatz, we find the equation

$$\lambda [\lambda + 2 - (2/n)]f(\theta) + f'(\theta) = 0.$$

Thus,

$$f(\theta) = A \sin \left(\sqrt{\lambda [\lambda + 2 - (2/n)]} \theta \right) + B \cos \left(\sqrt{\lambda [\lambda + 2 - (2/n)]} \theta \right).$$

By symmetry we know that the velocity must be mirrored across the x -axis, and therefore the solution can only be a cosine. Next we need the solution to be periodic over $0 \leq \theta \leq 2\pi$, which requires that

$$\sqrt{\lambda [\lambda + 2 - (2/n)]} = k, \quad \text{where } k = 0, 1, 2, 3 \dots$$

Hence, the eigenvalues are

$$\lambda_k = (1 - n)/n \pm \sqrt{[1 - (1/n)]^2 + k^2}. \quad (\text{B.1})$$

The full solution can then be written as an infinite series

$$U_z = \sum_{k=0}^{\infty} \left[a_k R^{(1-n)/n + \sqrt{[1 - (1/n)]^2 + k^2}} + b_k R^{(1-n)/n - \sqrt{[1 - (1/n)]^2 + k^2}} \right] \cos(k\theta).$$

The boundary conditions are

$$\left. \frac{\partial U_z}{\partial R} \right|_{R=1} = 0 \quad \text{and} \quad U_z(R=B) = B \cos(\theta).$$

Setting $k = 1$ and defining the positive root of the eigenvalue λ_1 , as λ_+ and the negative λ_- , we can write the second condition as

$$a_1 B^{\lambda_+} + b_1 B^{\lambda_-} = B.$$

The first boundary condition then gives

$$\left. \frac{\partial U_z}{\partial R} \right|_{R=1} = a_1 \lambda_+ + b_1 \lambda_- = 0.$$

Solving for b_1 we have

$$b_1 = -\frac{a_1 \lambda_+}{\lambda_-}.$$

Hence, we find that

$$a_1 = \frac{B/\lambda_+}{(B^{\lambda_+}/\lambda_+) - (B^{\lambda_-}/\lambda_-)} \cos(\theta) \quad \text{and} \quad b_1 = \frac{-B/\lambda_-}{(B^{\lambda_+}/\lambda_+) - (B^{\lambda_-}/\lambda_-)} \cos(\theta).$$

Now we can write the full solution as

$$U_z = B \frac{(R^{\lambda_+}/\lambda_+) - (R^{\lambda_-}/\lambda_-)}{(B^{\lambda_+}/\lambda_+) - (B^{\lambda_-}/\lambda_-)} \cos(\theta).$$

B.2 SCALING RELATIONSHIP FOR RADIAL AVERAGE VELOCITY

Here we give a more detailed derivation of the large S scaling for the average creep closure velocity \overline{U}_r . From equation (4.22), we have that

$$\overline{U}_r = -\frac{C}{R}.$$

Now the in-plane equilibrium equation averaged over θ is

$$\frac{\partial \overline{\Sigma}_{rr}}{\partial R} = \frac{\overline{\Sigma}_{\theta\theta} - \overline{\Sigma}_{rr}}{R}.$$

To find $\overline{\Sigma}_{rr}$, we need the term

$$\overline{\Sigma}_{\theta\theta} - \overline{\Sigma}_{rr} = -\frac{1}{\pi} \int_0^{2\pi} \dot{E}_E^{\frac{1}{n}-1} \dot{E}_{rr} d\theta. \quad (\text{B.2})$$

Breaking the strain rate up into θ -averaged and fluctuating components, we have that

$$\dot{E}_{rr} = \dot{\overline{E}}_{rr}(R) + \dot{E}'_{rr}(R, \theta). \quad (\text{B.3})$$

The ratio of these two terms are plotted in figure B.1 as a function of R , where the θ dependence of the fluctuating term is represented as a root mean square:

$$\text{rms} \left\{ \dot{E}'_{rr} \right\} (R) = \sqrt{\langle \dot{E}_{rr}'^2 \rangle_\theta (R)},$$

where angle brackets represent expectation. From figure B.1, we can see

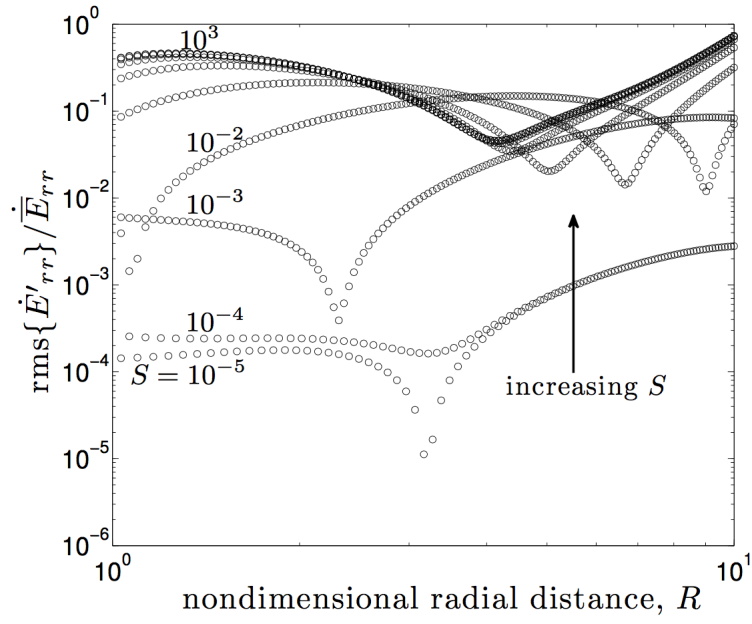


Figure B.1: Root mean square of deviations of \dot{E}_{rr} from mean strain rate \dot{E}_{rr} as a function of R for all S . The range of S is from $S = 10^{-5}$ (bottom circle line) to $S = 10^3$ (top circle line) in powers of ten. The outer radius of the domain is $B = 10$.

that the fluctuating terms are negligible for most values of S . Regardless, we can insert both terms from equation (B.3) into equation (B.2) and find that

$$\bar{\Sigma}_{\theta\theta} - \bar{\Sigma}_{rr} = -\frac{1}{\pi} S_n^{\frac{1}{n}-1} \dot{E}_{rr} \int_0^{2\pi} \left| \frac{1}{2} \nabla U_z \right|^{\frac{1}{n}-1} d\theta - \frac{1}{\pi} S_n^{\frac{1}{n}-1} \int_0^{2\pi} \left| \frac{1}{2} \nabla U_z \right|^{\frac{1}{n}-1} \dot{E}'_{rr} d\theta.$$

Inserting this into the average equilibrium equation, and using the average creep closure found earlier, we have that

$$\frac{\partial \bar{\Sigma}_{rr}}{\partial R} = -S_n^{\frac{1}{n}-1} \frac{C}{\pi R^3} \int_0^{2\pi} \left| \frac{1}{2} \nabla U_z \right|^{\frac{1}{n}-1} d\theta - \frac{S_n^{\frac{1}{n}-1}}{\pi R} \int_0^{2\pi} \left| \frac{1}{2} \nabla U_z \right|^{\frac{1}{n}-1} \dot{E}'_{rr} d\theta.$$

Integrating from $R = 1$ to $R = B$, where at $R = 1$, we have that $\bar{\Sigma}_{rr} = 1$, and, thus,

$$S_n^{\frac{n-1}{n}} = \frac{C}{\pi} \int_1^B \int_0^{2\pi} \frac{\left| \frac{1}{2} \nabla U_z \right|^{\frac{1}{n}-1}}{R^4} R d\theta dR + \frac{1}{\pi} \int_1^B \int_0^{2\pi} \frac{\left| \frac{1}{2} \nabla U_z \right|^{\frac{1}{n}-1}}{R^2} \dot{E}'_{rr} R d\theta dR \quad (\text{B.4})$$

We now refer to the two integrals as \mathcal{H} and \mathcal{J} , that is

$$\begin{aligned} \mathcal{H} &= \int_1^B \int_0^{2\pi} \frac{\left| \frac{1}{2} \nabla U_z \right|^{\frac{1}{n}-1}}{R^4} R d\theta dR, \\ \mathcal{J} &= \int_1^B \int_0^{2\pi} \frac{\left| \frac{1}{2} \nabla U_z \right|^{\frac{1}{n}-1}}{R^2} \dot{E}'_{rr} R d\theta dR, \end{aligned}$$

each of which is a constant that is a function of n and B as all θ and R dependence is integrated out. Thus, we can write out equation (B.4) as

$$C = \frac{\pi}{\mathcal{H}} S^{\frac{n-1}{n}} - \frac{\mathcal{I}}{\mathcal{H}}.$$

Inserting this into the creep closure at $R = 1$, we have that

$$\overline{U}_r = -\frac{\pi}{\mathcal{H}} S^{\frac{n-1}{n}} + \frac{\mathcal{I}}{\mathcal{H}}.$$

As previously mentioned, from figure B.1 we can see that the second term is much smaller than the first because $S \gg 1$ and \dot{E}'_{rr} is a small deviation from the average. If we neglect the second term, we can see that the average creep closure velocity, in absolute value, scales as

$$-\overline{U}_r \sim S^{\frac{n-1}{n}},$$

which matches our previous scaling exactly and is numerically corroborated in figure 4.7.

References

- [1] S. Adhikari and V. C. Tsai. A new model for subglacial flooding during the rapid drainage of supraglacial lakes. *AGU Fall Meeting*, 2014.
- [2] S. Adhikari and V. C. Tsai. A model for subglacial flooding through a preexisting hydrological network during the rapid drainage of supraglacial lakes. *J. Geophys. Res.*, 120, doi: 10.1002/2014JF003339 2015.
- [3] J.L. Bamber, R.B. Alley, and I. Joughin. Rapid response of modern day ice sheets to external forcing. *Earth and Planetary Science Letters*, 257(1):1–13, 2007.
- [4] G.I. Barenblatt. *Scaling, Self-similarity, and Intermediate Asymptotics*. Cambridge University Press, 1996.
- [5] T.C. Bartholomous, R.S. Anderson, and S.P. Anderson. Growth and collapse of the distributed subglacial hydrologic system of kennicott glacier, alaska, usa, and its effects on basal motion. *J. Glaciol.*, 57(206):985–1002, 2011.
- [6] A. F. Bower, N. A. Fleck, A. Needleman, and N. Ogbanna. Indentation of a power law creeping solid. *Proc. Roy. Soc. London Ser. A*, 441 (911):97–124, 1993.
- [7] G.K.C. Clarke. Hydraulics of subglacial outburst floods: new insights from the spring-hutter formulation. *Journal of Glaciology*, 49(165):299–313, 2003.
- [8] K.M. Cuffey and W.S.B. Paterson. *The physics of glaciers*. Academic Press, 2010.

- [9] M.C. Dallaston and I. Hewitt. Free-boundary models of a meltwater conduit. *Phys. Fluids*, 26(083101):1–21, 2014.
- [10] S.B. Das, I. Joughin, M.D. Behn, I.M. Howat, M.A. King, D. Lizarralde, and M.P. Bhatia. Fracture propagation to the base of the greenland ice sheet during supraglacial lake drainage. *Science*, 320(5877): 778–781, 2008.
- [11] Dassault. Abaqus user’s manual version 6.13-2. *Dassault Systèmes Simulia Corp., Providence, Rhode Island, USA*, 2013.
- [12] W.B. Durham, S.H. Kirby, and L.A. Stern. Creep of water ices at planetary conditions: A compilation. *J. Geophys. Res.*, 102(E7):16293–16302, 1997.
- [13] F. Erdogan, G. D. Gupta, and T. S. Cook. Numerical solution of singular integral equations. *Leyden, Noordhoff Int. Pub.*, Recent developments in fracture mechanics, G. C. Sih:368–425, 1973.
- [14] J.D. Eshelby. The determination of the elastic field of an ellipsoidal inclusion, and related problems. In *Proceedings of the Royal Society of London A: Mathematical, Physical and Engineering Sciences*, volume 241, pages 376–396. The Royal Society, 1957.
- [15] M.C. Fernandes, C.R. Meyer, T.Perol, and J.R. Rice. Röthlisberger channel model in ice stream shear margins and mountain glaciers accounting for anti-plane shear loading and undeforming bed. Abstract 1760 to be presented at 2015 IGS symposium on ice sheet hydrology, Iceland, 21–26 June., 2015.
- [16] A.G. Fountain and J.S. Walder. Water flow through temperate glaciers. *Rev. Geophys.*, 36:299–328, 1998.
- [17] D. I. Garagash and E. Detournay. Plane-strain propagation of a fluid-driven fracture: Small toughness solution. *J. Appl. Mech.*, 72: 916–928, 2005.
- [18] G. Gioia and P. Chakraborty. Turbulent friction in rough pipes and the energy spectrum of the phenomenological theory. *Phys. Rev. Lett.*, 96:1–4, 2006.

- [19] J.W. Glen. Measurement of the deformation of ice in a tunnel at the foot of an ice fall. *J. Glaciol.*, 2(20):735–745, 1956.
- [20] D.L. Goldsby and D.L. Kohlstedt. Superplastic deformation of ice: Experimental observations. *J. Geophys. Res.*, 106:11017–11030, 2001.
- [21] D.E. Hawk and J.L. Bassani. Transient crack growth under creep conditions. *Journal of the Mechanics and Physics of Solids*, 34(3): 191–212, 1986.
- [22] J.W. Hutchinson. Singular behaviour at the end of a tensile crack in a hardening material. *Journal of the Mechanics and Physics of Solids*, 16(1):13–31, 1968.
- [23] C.E. Inglis. Stresses in a plate due to the presence of cracks and sharp corners. *Trans. Inst. Naval Architects*, 55:219–241, 1913.
- [24] I. Joughin, S. Tulaczyk, R. Bindshadler, and S.F. Price. Changes in West Antarctic Ice Stream velocities: Observation and analysis. *J. Geophys. Res.*, 107(B11), 11 2002.
- [25] G. Kolosoff. Über einige eigenschaften des ebenen problems der elastizitätstheorie. *Zeitschrift für Mathematik und Physik*, 62:384–409, 1914.
- [26] I.L. Lim, I.W. Johnston, and S.K. Choi. Application of singular quadratic distorted isoparametric elements in linear fracture mechanics. *International journal for numerical methods in engineering*, 36(14):2473–2499, 1993.
- [27] M. McMillan, P. Nienow, A. Shepherd, T. Benham, and A. Sole. Seasonal evolution of supra-glacial lakes on the greenland ice sheet. *Earth and Planetary Science Letters*, 262(3):484–492, 2007.
- [28] A. Needleman and J. R. Rice. Plastic creep flow effects in the diffusive cavitation of grain boundaries. *Acta Metallurgica*, 28(10): 1315–1332, 1980.
- [29] J.F. Nye. The flow law of ice from measurements in glacier tunnels, laboratory experiments and the jungfraufirn borehole experiment.

Proceedings of the Royal Society of London. Series A. Mathematical and Physical Sciences, 219(1139):477–489, 1953.

- [30] T. Perol and J.R. Rice. Control of the width of West Antarctic ice streams by internal melting in the ice sheet near the margins. Abstract C11B-0677 presented at 2011 Fall Meeting, AGU, San Francisco, Calif., 5-9 Dec., 2011.
- [31] T. Perol, J.R. Rice, J.D. Platt, and J. Suckale. Stabilizing mechanism for migration of western antarctic ice streams. *submitted to J. Geophys. Res.*, 2015.
- [32] J.R. Rice and G.F. Rosengren. Plane strain deformation near a crack tip in a power-law hardening material. *Journal of the Mechanics and Physics of Solids*, 16(1):1–12, 1968.
- [33] J.R. Rice and G.F. Rosengren. Plane strain deformation near a crack tip in a power-law hardening material. *Journal of the Mechanics and Physics of Solids*, 16(1):1–12, 1968.
- [34] J.R. Rice, V.C. Tsai, M.C. Fernandes, and J.D. Platt. Time scale for rapid draining of a surficial lake into the greenland ice sheet. *Journal of Applied Mechanics*, 2015.
- [35] H. Röthlisberger. Water pressure in intra- and subglacial channels. *J. Glaciol.*, 11(62):177–203, 1972.
- [36] H. Rubin. *Environmental fluid mechanics*. CRC Press, 2001.
- [37] R.L. Shreve. Movement of water in glaciers. *J. Glaciol.*, 11(62):205–214, 1972.
- [38] K. Tinkler and J. Marsh. Niagara river. *The Canadian Encyclopedia*, February 2006.
- [39] V. C. Tsai and J. R. Rice. Modeling turbulent hydraulic fracture near a free surface. *J. Appl. Mech.*, 79(3), May 2012.
- [40] V.C. Tsai and J.R. Rice. A model for turbulent hydraulic fracture and application to crack propagation at glacier beds. *Journal of Geophysical Research: Earth Surface (2003–2012)*, 115(F3), 2010.

- [41] R.C. Viesca and J.R. Rice. Elastic reciprocity and symmetry constraints on the stress field due to a surface-parallel distribution of dislocations. *Journal of the Mechanics and Physics of Solids*, 59(4): 753–757, 2011.
- [42] V. Vitek. A theory of the initiation of creep crack growth. *International Journal of Fracture*, 13(1):39–50, 1977.
- [43] S. W. Vogel, S. Tulaczyk, B. Kamb, H. Engelhardt, F. D. Carsey, A. E. Behar, A. L. Lane, and I. Joughin. Subglacial conditions during and after stoppage of an Antarctic Ice Stream: Is reactivation imminent? *Geophys. Res. Lett.*, 32, 2005.
- [44] J.S. Walder. Röthlisberger channel theory: its origins and consequences. *J. Glaciol.*, 56(200):1079–1086, 2010.
- [45] J. Weertman. General theory of water flow at base of a glacier or ice sheet. *Rev. Geophys. Space Phys.*, 10:287–333, 1972.
- [46] J. Weertman. Can a water-filled crevasse reach the bottom surface of a glacier? *International Association of Hydrologic Sciences, IAHS 095 0139*:139–145, 1973.